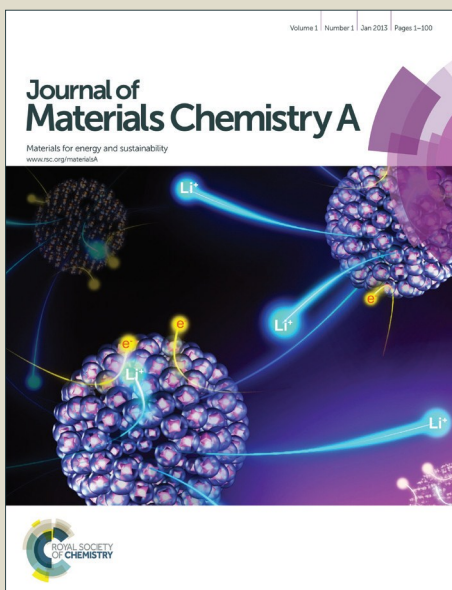


# Journal of Materials Chemistry A

Accepted Manuscript



This is an Accepted Manuscript, which has been through the Royal Society of Chemistry peer review process and has been accepted for publication.

Accepted Manuscripts are published online shortly after acceptance, before technical editing, formatting and proof reading. Using this free service, authors can make their results available to the community, in citable form, before we publish the edited article. We will replace this Accepted Manuscript with the edited and formatted Advance Article as soon as it is available.

You can find more information about Accepted Manuscripts in the [Information for Authors](#).

Please note that technical editing may introduce minor changes to the text and/or graphics, which may alter content. The journal's standard [Terms & Conditions](#) and the [Ethical guidelines](#) still apply. In no event shall the Royal Society of Chemistry be held responsible for any errors or omissions in this Accepted Manuscript or any consequences arising from the use of any information it contains.

# Recent Advances in Heterogeneous Electrocatalysts for Hydrogen Evolution Reaction

Min Zeng, Yanguang Li\*

Institute of Functional Nano & Soft Materials, Soochow University, Suzhou 215123, China

Correspondence to yanguang@suda.edu.cn

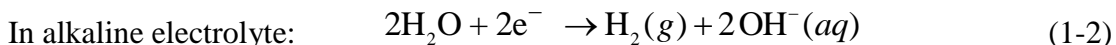
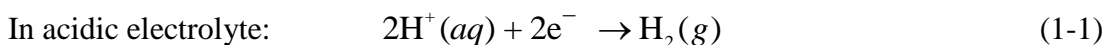
## Abstract

Hydrogen evolution reaction plays a decisive role in a range of electrochemical and photoelectrochemical devices. It requires efficient and robust electrocatalysts to lower the reaction overpotential and minimize energy consumption. Over the last decade, we have witnessed a rapid rise of new electrocatalysts, particularly those based on non-precious metals. Some of them approach the activity of precious metal benchmarks. Here, we present a comprehensive overview of the recent developments of heterogeneous electrocatalysts for hydrogen evolution reaction. Detailed discussion is organized from precious metals to non-precious metal compounds including alloys, chalcogenides, carbides, nitrides, borides and phosphide, and finally to metal-free materials. Emphasis is placed on the challenges facing these electrocatalysts and solutions for further improving their performance. We conclude with a perspective on the development of future HER electrocatalysts.

## 1. Introduction

Over recent years, there has been increasing emphasis on renewable energy sources as alternatives to fossil fuels for their smaller ecological footprints. Since the early seventies of the last century, hydrogen has been advocated as the ideal energy carrier by virtue of its highest gravimetric energy density of any known fuel with zero emission of carbon dioxide.<sup>1-5</sup> It can store energy produced from renewable sources in the form of chemical bonds, and then be transported to end-users for converting back to electricity on fuel cells or other devices when needed. On our planet, hydrogen is not available in free form, but mainly exists in compounds such as hydrocarbons and water. At present, it is predominantly obtained from the steam reforming of hydrocarbons — an energy intensive and greenhouse gas emission intensive process.<sup>6</sup> Its sustainable production on an economical and industrial scale presents a daunting challenge. One proposed approach to accomplish this is via electrolytic or photocatalytic water splitting in which water molecules are dissociated into their constituent parts using the renewable power of sunlight, either directly or indirectly.<sup>2-5</sup>

Hydrogen evolution reaction (HER) is the cathodic half reaction of water splitting, and is one of the most well-studied electrochemical reactions. It is pivotal to a range of energy conversion devices including water electrolyzers and artificial photosynthetic cells.<sup>3-5</sup> As illustrated by the following equations, it proceeds through the reduction of protons or water molecules accompanied by the subsequent evolution of gaseous hydrogen just as its name implies. The standard reduction potential of HER is defined as  $E_{H^+/H_2O}^o = 0$  V versus normal hydrogen electrode at pH = 0. Nevertheless, similar to many chemical reactions, electrochemical processes have to surmount certain activation energy barrier (known as overpotential in electrochemistry) to occur. They usually demand the assistance of electrocatalysts to lower the overpotential, and consequently promote the reaction rate and efficiency.



Electrocatalysts can be generally categorized as either homogeneous or heterogeneous depending on whether or not they function in the same phase as the reactants. Examples of homogeneous HER electrocatalysts are water-soluble molecular and enzymatic electrocatalysts such as hydrogenase.<sup>7-9</sup> Heterogeneous HER electrocatalysts are usually water-insoluble solids. They have to be directly mounted onto the working electrode for use. People have a long history of using heterogeneous HER electrocatalysts. When electrolysis was early introduced by Nicholson and Carlisle in 1800, two platinum wires were used as working electrodes in a sealed tube filled with water and powered by a voltaic pile.<sup>10, 11</sup> They observed a stream of bubbles on both electrodes, which were later identified to be hydrogen and oxygen. After more than two centuries, platinum and platinum group metals remain the most efficient HER electrocatalysts capable of driving significant currents close to the thermodynamic potential.<sup>5, 12</sup> Even though in alkaline electrolytes nickel and nickel alloys can marginally rival platinum group metals in activity and are frequently used as the cathode in today's alkaline electrolyzers,<sup>11, 13, 14</sup> platinum is the HER electrocatalyst of the choice for acidic proton exchange membrane electrolyzers which are more favored for their compact structures. However, platinum group metals all suffer from high cost. Their scarcity also determines that they will not benefit from economies of scale, and therefore are not viable for large scale industrial applications. Attention now is shifted toward low-cost alternatives. Over the past decade, tremendous efforts have been actively engaged in this area with many exciting progresses, part of them have been previously accounted in some excellent reviews.<sup>5, 15-17</sup> Nevertheless, in light of the latest increased research activities, an up-to-date and comprehensive account of current status and challenges of HER electrocatalysis becomes necessary.

Here we present a review of heterogeneous HER electrocatalysts with an emphasis on those made of non-precious metal compounds. We start with a brief introduction of HER electrocatalysis covering some basic concepts, thermodynamics and possible reaction pathways. It is followed by detailed discussions on different HER electrocatalysts grouped based on their compositions: from

precious metals to non-precious metal compounds, including alloys, chalcogenides, carbides, nitrides, borides and phosphides, and finally to metal-free HER catalysts in sequential order. For each type of catalysts, we summarize major achievements and discuss prevailing trends for improving their performance. At last, we present a perspective on the development of future HER electrocatalysts. With these, we hope to provide readers with a glimpse of this rapidly evolving field.

## 2. Fundamentals of HER

Under standard conditions ( $T = 298\text{ K}$ ,  $P_{\text{H}_2} = 1\text{ atm}$ ), the Nernstian potential for HER referenced to normal hydrogen electrode (NHE) is described by Equation 2-1. It is pH-dependent and shifts linearly by -59 mV for each pH unit increase. Such pH dependence can be annulled when referenced to reversible hydrogen electrode (RHE). On the RHE scale, the Nernstian potential for HER is straightforward and equals zero regardless of electrolytes in use.

$$E_{\text{HER}} = E_{(\text{H}_2/\text{H}^+)}^0 - \frac{RT}{F} \times \ln(a_{\text{H}^+}/P_{\text{H}_2}^{1/2}) = -0.059 \times (\text{pH}) \text{ V vs. NHE} = 0 \text{ V vs. RHE} \quad (2-1)$$

The Nernstian potential reflects the thermodynamic equilibrium potential at which the electrochemical reaction under study can take place. However, in practice HER is rarely initiated at its equilibrium potential. This can be understood as most electrochemical processes have to overcome certain activation energy barrier to proceed as schematically illustrated by Figure 1A.<sup>16, 18</sup> The height of energy barrier is largely determined by the nature of interface on which reactions occur. Consequently, electrochemical reactions usually demand extra energy than dictated by thermodynamics. HER doesn't start until a sufficiently cathodic potential is applied with reaction overpotentials (defined as the difference between equilibrium potential and applied potential) sometimes up to >1 V (Figure 1B). Taking this into consideration, the potential to drive HER can be expressed as:

$$E_i = E_{\text{HER}} + iR + \eta \quad (2-2)$$

where  $iR$  is the ohmic potential drop caused by flow of current in ionic electrolyte and  $\eta$  is the reaction overpotential. Overpotential is one of the most important electrode parameters to evaluate its electrochemical performance. The smaller overpotential, the higher energy efficiency. For practical applications, HER electrocatalysts are often employed to lower reaction overpotential as much as possible by activating the intermediate chemical transformation. In general, desired HER electrocatalysts should be capable of catalyzing the reaction within 100 mV overpotential or less.

The kinetics of HER is more complex. It is strongly dependent on the electrochemical potential, given by the Butler-Volmer equation as shown below:<sup>19, 20</sup>

$$j = j_0 \left[ -e^{-\alpha nF\eta/RT} + e^{(1-\alpha)nF\eta/RT} \right] \quad (2-3)$$

where  $j$  is the current density,  $j_0$  is the exchange current density,  $\alpha$  is the charge transfer coefficient,  $n = 1$  is the number of electrons transferred,  $F$  is the Faraday constant,  $R$  is the ideal gas constant, and  $T$  is the temperature. The exchange current density describes the rate of reaction at the equilibrium potential, and is another key electrode parameter in the evaluation of electrocatalytic activity. For platinum, the exchange-current density is generally found to be in the range  $j_0 = 10^{-4} \sim 10^{-2}$  A/cm<sup>2</sup> depending on the electrolyte and its purity.<sup>21</sup> When the overpotential is small ( $\eta < 0.005$  V), the Butler-Volmer equation can be simplified as:

$$\eta = \left( \frac{RT}{nFj_0} \right) j \quad (2-4)$$

It indicates that the overpotential is linearly correlated to the current density within a narrow potential range near the equilibrium potential. At higher overpotential ( $\eta > 0.05$  V), the Butler-Volmer equation can be simplified as the Tafel equation:

$$\eta = a + b \log j = \frac{-2.3RT}{\alpha nF} \log j_0 + \frac{2.3RT}{\alpha nF} \log j \quad (2-5)$$

This equation shows a linear relationship between the overpotential and  $\log j$ , with a slope  $b = \frac{2.3RT}{\alpha nF}$  termed the Tafel slope. Tafel slope is commonly used to discern the rate determining

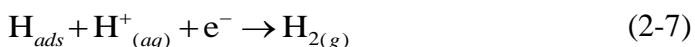
step and possible HER reaction pathway as will be discussed in detail later in this section. Practically, Tafel slope suggests the overpotential increment necessary to raise the current density by ten-fold. A small Tafel slope corresponds to a steep rise of the electrocatalytic current density. Experimentally, one can perform Tafel analysis of the electrode polarization curves to derive kinetic information including exchange current density and Tafel slope.

Ideal catalysts should have small overpotentials, low Tafel slopes and large exchange current densities. However, these parameters are not entirely independent of each other. For instance, HER electrocatalysts with lower Tafel slopes more often exhibit smaller exchange current densities, and vice versa as schematically shown in Figure 1B and 1C. Under these circumstances, a better electrocatalyst is always the one having a smaller overpotential at the targeted current density. For HER, the figure of merit used to quantify electrocatalytic activity is usually the potential to achieve a current density of  $10 \text{ mA/cm}^2$  — a value relevant to solar fuel synthesis.<sup>22</sup>

The HER kinetics is strongly influenced by its reaction pathway, which can be both catalyst-dependent and potential-dependent. Sometimes, more than one pathway can be simultaneously operative on a single electrocatalyst owing to the existence of different surface crystalline facets. There is a general consensus that HER in acidic electrolytes consists of two primary steps.<sup>23</sup> In the first step, a proton-coupled electron transfer at the catalyst surface yields an intermediate adsorbed hydrogen atom. This step is known as the discharge reaction or Volmer reaction:



Subsequent hydrogen desorption may proceed through two possible pathways. The adsorbed hydrogen atom can react with another proton from the solution accompanied by a second electron transfer to form molecular hydrogen. This possible step is known as the electrochemical desorption reaction or Heyrovsky reaction:



Another possibility is the combination of two adsorbed hydrogen atoms to form molecular hydrogen, known as the recombination reaction or Tafel reaction.



It is challenging to elucidate the exact operating mechanism on different HER electrocatalysts. However, the Tafel slope can be usually taken as an indication of the rate determining step, and may provide some valuable insight into possible reaction pathways.<sup>19, 20, 23</sup> From Butler-Volmer kinetics, it can be deduced that the Tafel slope is 118 mV/decade, 39 mV/decade or 29.5 mV/decade when the discharge reaction (2-6), electrochemical desorption reaction (2-7) or recombination reaction (2-8) is rate-determining, respectively. For platinum, experimental results obtained in acid solutions indicate that at low overpotentials the recombination reaction is rate-determining following the fast initial discharge step.<sup>20</sup> A Tafel slope  $b \sim 30$  mV/decade is measured at this potential range. As the overpotential is increased, the coverage of absorbed hydrogen atom approaches saturation. This leads to accelerated atom-atom recombination. As a result the discharge step becomes rate-determining with a measured Tafel slope  $b \sim 120$  mV/decade.<sup>20</sup>

From above discussions, we can see that hydrogen adsorption and desorption on the electrode surface are two successive steps in HER electrocatalysis. However, they are competitive in nature: a catalyst surface having too weak bonding strength with hydrogen atom cannot efficiently adsorb the reactant to initiate HER, whereas a catalyst surface having too strong bonding strength would have difficulty in releasing the product toward the completion of HER. Therefore, ideal HER electrocatalysts should have well-balanced hydrogen bonding and releasing properties.<sup>24, 25</sup> This is in line with Sabatier principle which states that in heterogeneous catalysis and electrocatalysis optimal catalytic activity can be achieved on a catalytic surface having intermediate bonding energies with reactive intermediates.<sup>26</sup> In 1958, Parson first pointed out that the maximum exchange current density is attained when hydrogen adsorption free energy is close to thermoneutral ( $\Delta G_H \sim 0$ ).<sup>27</sup> Using density functional theory, Norskov and co-workers calculated hydrogen adsorption free energy

on different transition metals.<sup>24</sup> When experimentally measured HER exchange current density was plotted as a function of the calculated free energy, an interesting volcano-shaped curve was obtained with the peak position close to platinum (Figure 2). They suggested that  $\Delta G_H$  is a useful descriptor in the selection of new electrocatalysts for hydrogen evolution as well as for hydrogen oxidation reaction. Following this principle, Norskov and co-workers predicted high HER activity of BiPt surface alloys and edge sites on layered MoS<sub>2</sub>.<sup>25, 28</sup> These predictions were borne out by subsequent electrochemical measurements.

Hydrogen adsorption free energy is an intrinsic property of electrocatalysts. However, it should be noted that in practice the activity of a HER electrocatalyst is collectively influenced by many other factors as well including but not limited to conductivity, crystallinity, roughness and catalyst supports. It may vary significantly even for the same catalyst material prepared by different methods. These factors are difficult to be captured by theory. Over the last decade of active research, much experience has been accumulated regarding structural and compositional engineering of electrocatalysts to preferentially expose active sites and/or to promote site-specific activities. Nanostructured HER electrocatalysts in a variety of forms and dimensions have been made with greatly improved electrochemical performance compared to their bulk counterpart on gravimetric basis. They are the focus of the discussion in the ensuing sections. Table 1 lists and compares their HER performance.

### 3. HER Electrocatalysts

#### 3.1 Precious metal based electrocatalysts

Platinum group metals (PGMs, including Pt, Ru, Rh, Ir and Pd) are the best known HER electrocatalysts located close to the apex of the volcano plot (Figure 2). Among them, Pt is the most popular choice, and frequently used to benchmark the activity of other HER electrocatalysts. Unfortunately, the widespread applications of PGM catalysts are prohibited by their high cost and

low abundance. Two general strategies have been sought to tackle with this problem. The first one is to use microstructured or nanostructured electrocatalysts with large surface to volume ratio. Since electrocatalysis is a surface process, efficient utilization of surface catalytic atoms can significantly alleviate the demand on high catalyst loading. Over the past decade, the progress in materials science and nanotechnology has greatly accelerated the development of PGM nanostructures with controllable sizes and shapes.<sup>29</sup> Engineering porosity in PGM nanostructures has also been proven an effective approach to improve their electrocatalytic performance by facilitating the mass transport of reactant molecules.<sup>30, 31</sup> To explore the possible lower limit of catalyst loading, Chen *et al.* proposed to use monolayer Pt supported on low-cost materials as alternatives to PGM electrocatalysts (Figure 3). WC was favored as the support material since it has similar bulk electronic properties to Pt, as suggested by density functional theory calculations.<sup>32-34</sup> They demonstrated that Pt monolayer on bulk WC had comparable activity to that of bulk Pt, whilst an order of magnitude reduction in Pt loading and cost was achieved. These results showed that all but outmost layer of Pt atoms could be replaced by WC without compromising electrocatalytic activity. The method was further extended to other metal overlayers (Pd and Au) and supports (Mo<sub>2</sub>C). Resulting electrocatalysts exhibited excellent HER activity and stability in acidic environment.<sup>34, 35</sup>

The second strategy is to alloy PGMs with other metals so as to increase their site-specific activity, thereby allowing for lower catalyst loading to be used.<sup>25</sup> Alloys usually possess chemical and physical properties distinct from pure metals. To search for active and stable binary alloys for HER electrocatalysis, Nøskov *et al.* applied a high-throughput computational screening procedure based on DFT to the evaluation of more than 700 binary alloys.<sup>25</sup> Among a number of interesting candidates identified, surface alloy formed from Pt and Bi was found to be the most promising. Calculations suggested that  $\Delta G_H$  for BiPt was ~0.04 eV closer to the thermoneutral compared to Pt, indicating that its HER activity should be comparable to, or even better than pure Pt. The authors further prepared the targeted BiPt alloy via the underpotential deposition of a submonolayer of Bi on

Pt surface followed by annealing at mild temperatures. Thus formed surface alloy exhibited ~50% higher HER current density than initial Pt film, in good agreement with computational predictions. This example well illustrates the power and potential of combinatorial screening procedures. It makes an excellent complement to experimental assessments and can greatly expedite the discovery of new catalytic materials.

### 3.2 Non-precious metals and their alloys

In industrial alkaline electrolyzers, Ni-based electrodes are commonly employed as the cathode for the production of hydrogen because of their low cost and corrosion resistance at high pH values.<sup>11</sup> However Ni usually suffers from insufficient electrocatalytic activity and more importantly, progressive deactivation toward HER upon continuous alkaline electrolysis due to the reversible formation of nickel hydride species<sup>36, 37</sup>. Extensive efforts have been devoted to making Ni-based alloys for improved activity and durability. One example is Raney Ni, a material first developed in 1926 for the hydrogenation of vegetable oils.<sup>38, 39</sup> Raney Ni is derived from a Ni-Al alloy at specific concentration depending on desired properties. The alloy is leached in an alkaline solution to dissolve most of the Al-containing phase, leaving behind a porous Ni structure. Remaining Al can act as a matrix stabilizing the highly dispersed Ni for HER.

Besides Raney Ni, other Ni-based binary transition metal alloys have also been investigated. Vasu *et al.* electrodeposited Ni-Mo, Ni-Zn, Ni-Co, Ni-W, Ni-Fe and Ni-Cr alloys on steel strips and assessed their HER activities in alkaline solution.<sup>13</sup> They concluded that the Ni-Mo alloy was the most active and stable HER electrocatalyst with overpotential of ~0.18 V at 300 mA/cm<sup>2</sup> for over 1500 h of continuous electrolysis in 6 M KOH at 80 °C. The excellent electrocatalytic performance of Ni-Mo alloy can be rationalized by the hypo-hyper-d-electronic interactive effect in Brewer-type intermetallic systems, which predicts that when metals of the left half of the transition series having empty or half-filled d-electrons (*e.g.* Mo) are alloyed with metals of the right half of the transition

series having internally paired d-electrons (*e.g.* Ni), a well pronounced synergism in electrocatalytic activity for HER arises, often exceeding the catalytic power of precious metals.<sup>40</sup> Following their initial work, Vasu *et al.* further explored Ni-Mo-X ternary transition metal alloys and found that Ni-Mo-Fe had the most encouraging long term stability and tolerance to electrochemical corrosion.<sup>41</sup> More recently, Gray *et al.* reported the preparation of unsupported Ni-Mo nanopowders as an efficient HER electrocatalyst at room temperature (Figure 4).<sup>42</sup> Contrary to electrodeposited films, the alloy nanopowders could be suspended in common solvents and then cast onto arbitrary substrates for use. This electrocatalyst displayed excellent HER activity under alkaline conditions and was among the most active non-precious metal based HER catalysts. As shown in Figure 3c, at a catalyst loading of 1 mg/cm<sup>2</sup>, less than 100 mV overpotential is needed to sustain current densities in excess of 10 mA/cm<sup>2</sup> in 1 M NaOH. Sun *et al.* electrodeposited Ni-Mo alloys onto Cu foam to take advantage of the large surface area, porous current collector.<sup>43</sup> They showed that the overpotential was only ~34 mV at the cathodic current density of 20 mA/cm<sup>2</sup> in 1 M NaOH, even outperforming the Pt benchmark. The electrocatalyst also exhibited good performance stability without obvious loss of HER current density after 1000 potential cycles.

Other than alloying, the HER performance of transition metals in alkaline solution may also be boosted through hybridization with other functional materials. It has been recognized that the activities of most HER electrocatalysts in alkaline electrolytes are usually about two to three orders of magnitude lower than in acids because of the inefficient water dissociation step in alkaline medium.<sup>44, 45</sup> This limit may be lifted by introducing a second functional component, usually oxides or hydroxides, to promote the cleavage of water and the generation of reactive hydrogen intermediates which subsequently adsorb on nearby transition metal sites and further react to form molecular hydrogen.<sup>44, 45</sup> Guided by this design principle, Markovic *et al.* examined 9 different transition metals (both precious and non-precious ones) modified by Ni(OH)<sub>2</sub> clusters for HER in 0.1 M KOH.<sup>45</sup> They reported that the overpotentials on these bifunctional hybrids were dramatically

reduced by 200-500 mV compared to corresponding transition metals alone. In addition, the reactivity trends on  $\text{Ni(OH)}_2$ /transition metal catalysts was observed to be very similar to the volcano curve established in acid solution, implying that the water dissociation step was no longer rate-limiting at the presence of  $\text{Ni(OH)}_2$  clusters. Dai *et al.* developed Ni/NiO core/shell heterostructures grown on carbon nanotube as highly efficient electrocatalysts for HER with activity close to Pt (Figure 5).<sup>46</sup> The heterostructure was formed via partial reduction of  $\text{Ni(OH)}_2$  at mild temperatures. In 1 M KOH, the hybrid catalyst loaded on Ni foam electrode with a high catalyst loading of  $8 \text{ mg/cm}^2$  was able to sustain a remarkable current density of  $100 \text{ mA/cm}^2$  at  $<100 \text{ mV}$  overpotential, significantly more active than pure Ni or its hybrid with carbon nanotubes (Figure 5c). Even though the authors did not explicitly highlight the synergism between Ni core and NiO shell, we conjecture that the oxide shell assists in the water dissociation in the same manner  $\text{Ni(OH)}_2$  does in the prior example, and thus facilitates the HER electrocatalysis on the metallic core. Combining this HER electrocatalyst and a highly active water oxidation electrocatalyst made of Ni-Fe layer double hydroxide (LDH) developed by the same group,<sup>47</sup> they successfully demonstrated an efficient alkaline electrolyzer delivering  $\sim 20 \text{ mA/cm}^2$  at a voltage of 1.5 V with good operation stability at 60 °C (Figure 5d).

In general, nonprecious metals and their alloys are not suited for HER in acids due to their rapid corrosion. However, it was recently demonstrated that graphene encapsulated metal nanoparticles are highly active in acidic environments.<sup>48, 49</sup> Within such core-shell structures, graphene shells protect metal nanoparticles from deactivation by corrosive electrolytes, while metals' electron density can effectively penetrate the shell and reach outmost surfaces for rapid electrocatalytic reactions as suggested by DFT calculations. One of the best such materials is single-shell graphene encapsulated Fe nanoparticles decorated on single-walled carbon nanotubes prepared from floating catalyst CVD process.<sup>49</sup> Its HER performance in 0.5 M  $\text{H}_2\text{SO}_4$  closely approaches that of the Pt benchmark with remarkable durability.

### 3.3 Transition metal chalcogenides

Transition metal chalcogenides have gained growing attention for use as HER electrocatalysts since about a decade ago. The most well-known example among them is MoS<sub>2</sub>. Following discussion focuses on this particular material to exemplify the quick development of chalcogenide-based HER electrocatalysts. MoS<sub>2</sub> possesses a layered structure analogous to graphite with weak van der Waals interactions between neighboring layers (Figure 6A). Historically, it has been used as a solid lubricant for its low friction properties and as a hydrodesulfurization catalyst to lower sulfur content in natural gas and fuels.<sup>50, 51</sup> Bulk natural crystals of MoS<sub>2</sub> were first examined as a possible HER electrocatalyst as early as 1977 by Tributsch *et al.*<sup>52</sup> However, it was not until about 20 years later that its potential in HER was fully unveiled. In 2005, Nørskov *et al.* applied density functional theory (DFT) calculations to analyze the free energy of hydrogen bonding to this layered material.<sup>28</sup> They noted that while the basal plane of MoS<sub>2</sub> was catalytically inert, its sulfided Mo-edges were active for HER with suitable  $\Delta G_H \sim 0.1$  V, close to those of several efficient HER electrocatalysts including Pt, nitrogenase and hydrogenase. The computational results were in good agreement with their experimental findings, which showed that nanosized MoS<sub>2</sub> clusters on a graphite support indeed had very decent HER activity with an overpotential in the range 0.1 ~ 0.2 V at pH = 0. In a subsequent study, Chorkendorff *et al.* prepared MoS<sub>2</sub> nanoparticles of different sizes on Au, and quantified the fraction of the terrace and edge sites using scanning tunnelling microscopy (Figure 6B).<sup>53</sup> Their electrochemical measurements revealed a linear dependence of HER exchange current density on the edge length of MoS<sub>2</sub> nanoparticles, thereby confirming that HER active sites were located on the edges (Figure 6C). To compare the HER activity of MoS<sub>2</sub> to other materials on a per active site basis, the authors estimated the turnover frequency (TOF) of MoS<sub>2</sub> edges to be 0.02 s<sup>-1</sup>, not much lower than that of Pt (111) surface (0.9 s<sup>-1</sup>).

Inspired by these two seminal works, research on MoS<sub>2</sub> for HER has been on a continuous rise, most rapidly since 2011.<sup>15, 54-57</sup> From the thermodynamic point of view, edges of layered materials

are not favourable surface sites due to their inherently higher surface energy. Most MoS<sub>2</sub> nanomaterials tend to form close-shell fullerene structures with the termination of electrocatalytically inert basal planes.<sup>58, 59</sup> To tackle with this challenge, considerable efforts have been invested on the structural engineering of MoS<sub>2</sub> materials to preferentially expose their active edges. For example, Jaramillo *et al.* synthesized contiguous large-area thin films of a highly ordered double-gyroid MoS<sub>2</sub> network by templating mesoporous silica films (Figure 6D).<sup>60</sup> The high surface curvature and large surface area associated with the double-gyroid morphology was expected to engender more exposed edge sites. These films exhibited an HER onset overpotential of 150-200 mV, and a Tafel slope of 50 mV/decade. Xie *et al.* reported a scalable approach to engineer defects on the basal plane of MoS<sub>2</sub> nanosheets.<sup>61</sup> Excess thiourea added during the chemical synthesis was found responsible for the formation of defective structures, giving rise to the exposure of approximately 3 times more active edge sites. Resulting defect-rich MoS<sub>2</sub> nanosheets exhibited a small HER onset overpotential of 120 mV, a large cathodic current density of 13 mA/cm<sup>2</sup> at  $\eta = 200$  mV, and a small Tafel slope of 50 mV/decade, all much improved compared to defect-free MoS<sub>2</sub> nanosheets. Cui *et al.* demonstrated a rapid sulfurization process to convert Mo thin films deposited on various substrates to MoS<sub>2</sub> films.<sup>62</sup> Most interestingly, these MoS<sub>2</sub> films were terminated with vertically aligned edges — a structural feature ideal for HER electrocatalysis (Figure 6E). The authors recorded a large exchange current density of  $2.2 \times 10^{-6}$  A/cm<sup>2</sup> and a TOF  $\sim 0.013$  s<sup>-1</sup>.

Using proper functional substrate can also stabilize the formation of MoS<sub>2</sub> particles with nanoscale dimensions and abundant edges. Dai *et al.* developed a solvothermal method to prepare MoS<sub>2</sub>/graphene hybrid material using (NH<sub>4</sub>)<sub>2</sub>MoS<sub>4</sub> and graphene oxide nanosheets as the starting precursors (Figure 6F).<sup>63</sup> During the reaction, oxygen functionalities of graphene oxide nanosheets induced the selective growth of edge-rich MoS<sub>2</sub> nanoparticles on nanosheets. Electrochemical measurements showed that the hybrid catalyst had remarkable HER activity with an improved onset overpotential of  $\sim 100$  mV and a Tafel slope as small as  $\sim 40$  mV/decade. Based on the discussion in

Section 2, a Tafel slope of 40 mV/decade strongly supported that HER electrocatalysis on the hybrid catalyst followed the Volmer-Heyrovsky pathway with the electrochemical desorption reaction as the rate determining step. In addition to high activity, this material also exhibited satisfactory durability. Negligible loss of the cathodic current was observed after 1000 potential cycles.

Other than structural engineering, it has been recently recognized that the crystal structure of MoS<sub>2</sub> can drastically impact its HER activity. MoS<sub>2</sub> has two common polytypes: the hexagonal 2H-MoS<sub>2</sub> built from edge-sharing MoS<sub>6</sub> trigonal prisms and the tetragonal 1T-MoS<sub>2</sub> composed of edge-sharing MoS<sub>6</sub> octahedra (Figure 6A).<sup>64</sup> The 2H-polytype is more stable, and is the dominant structure adopted by most (if not all) chemically synthesized MoS<sub>2</sub> materials. On the other hand, the 1T-polytype so far is usually prepared through the intercalation of 2H-MoS<sub>2</sub> host lattices by alkali metals such as Li. Subsequent solvation of these intercalates leads to the exfoliation and release of free 1T-MoS<sub>2</sub> layers. It is suggested that the 1T-polytype is metallic and electrocatalytically more active than the semiconducting 2H-polytype. For example, in the study by Jin *et al.*, 1T-MoS<sub>2</sub> nanosheets exfoliated after Li chemical interaction delivered a HER current density of 10 mA/cm<sup>2</sup> at an overpotential of 187 mV while the same current density could not be reached until a much larger overpotential of 320 mV was applied for 2H-MoS<sub>2</sub> nanosheets.<sup>65</sup> Li intercalation into MoS<sub>2</sub> layered structure can also be achieved electrochemically in a battery configuration with a precise control of the intercalation degree. Using this strategy, Cui *et al.* demonstrated that the ratio of 2H to 1T phase of MoS<sub>2</sub> could be progressively tuned, and that its HER activity was significantly improved by lower voltage Li intercalation.<sup>66</sup> Despite its more advantageous electrocatalytic properties, the applicability of 1T-MoS<sub>2</sub> for HER unfortunately is mainly limited by the tedium of its preparation and its metastability only below 95°C.<sup>67</sup>

Moreover, amorphous MoS<sub>x</sub> materials have also been investigated for HER with some success.<sup>68-71</sup> Amorphous materials usually require no high-temperature processing. They lack long-range structural order, and the resulting defects may serve as efficient electrocatalytic centers.

Hu *et al.* prepared amorphous MoS<sub>x</sub> films by electrodeposition from an aqueous solution of (NH<sub>4</sub>)<sub>2</sub>MoS<sub>4</sub> on different conductive substrates.<sup>69</sup> These electrocatalysts were operative within a wide range of electrolyte pHs (*e.g.* 0 to 13). In 1 M H<sub>2</sub>SO<sub>4</sub>, they were shown to have a Tafel slope of 40 mV/decade and sustain a cathodic current density of 14 mA/cm<sup>2</sup> at  $\eta = 200$  mV. In a parallel study, Jaramillo *et al.* reported a wet chemical synthesis of nanostructured amorphous MoS<sub>x</sub> by reacting ammonium heptamolybdate and Na<sub>2</sub>S within a H<sub>2</sub>SO<sub>4</sub> solution.<sup>70</sup> The overpotential for this catalyst to achieve 10 mA/cm<sup>2</sup> was about 200 mV and the average Tafel slope for this catalyst was 60 mV/decade.

The third tactic to improve the HER performance of MoS<sub>2</sub> is combined with other metal cations as promoters. In hydrodesulfurization reactions, Co or Ni is often used to promote the catalytic activity of MoS<sub>2</sub>. Effects of their incorporation on structural and catalytic properties have been extensively studied, and it is widely accepted that promoter atoms are located at the S-edges.<sup>72</sup> Chorkendorff *et al.* performed DFT calculations to show that the free energy of hydrogen adsorption for S-edges decreased from 0.18 to 0.10 eV upon the incorporation of Co, which was close to the 0.08 eV for Mo-edges.<sup>73</sup> It indicated that the normally less active S-edges became more active in the presence of Co, thus promoting the overall density of active sites. Electrochemical measurement showed that Co-promoted MoS<sub>2</sub> had more than twice larger HER current density than pristine MoS<sub>2</sub>.

Following the success of MoS<sub>2</sub>, research attention has also been extended to several other layered transition metal chalcogenides or chalcogenide alloys.<sup>74</sup> WS<sub>2</sub> is isostructural to MoS<sub>2</sub>, and they two share a set of physical and chemical properties. It is therefore not surprising that experience accumulated from MoS<sub>2</sub> HER as previously reviewed can be transplanted or adapted to WS<sub>2</sub>. Chhowalla *et al.* reported exfoliated WS<sub>2</sub> nanosheets from Li chemical intercalation as efficient HER electrocatalyses.<sup>75</sup> The lowest Tafel slope of exfoliated nanosheets was ~60 mV/decade (or ~55 mV/decade after iR correction) in 0.5 M H<sub>2</sub>SO<sub>4</sub>. They had an exchange current density of  $\sim 2 \times 10^{-5}$

A/cm<sup>2</sup> and a TOF of 0.043 s<sup>-1</sup>. Analyses indicated that the enhanced electrocatalytic performance was associated with the high concentration of the strained metallic 1T phase. The chemical intercalation of Li is known to be more difficult for WS<sub>2</sub> than MoS<sub>2</sub>.<sup>76</sup> To expedite this process, Jin *et al.* developed a facile microwave-assisted intercalation method that shortened the reaction time from 48 h to 20 min.<sup>77</sup> Exfoliated 1T-WS<sub>2</sub> nanosheets were able to deliver a HER current density of 10 mA/cm<sup>2</sup> at a low overpotential of 142 mV. Very recently, our group demonstrated a high-temperature solution-phase method for the synthesis of WS<sub>2</sub> nanoflakes (Figure 7A).<sup>78</sup> Spectroscopic and microscopic characterizations showed the product was mostly comprised of monolayered nanoflakes about 5-20 nm in size that loosely stacked together to form larger primary particles (Figure 7B,C). The nanoflake catalyst achieved 10 mA/cm<sup>2</sup> at  $\eta \sim 160$  mV and a Tafel slope of about 48 mV/decade (Figure 7D). Furthermore, the catalyst showed excellent operation stability. The overpotential to sustain 10 mA/cm<sup>2</sup> only increased ~15 mV after extended potential cycling of 10000 cycles (Figure 7E).

The selenium analogues — MoSe<sub>2</sub> and WSe<sub>2</sub> are also active for HER. Nørskov *et al.* used DFT calculations to determine the free energy of hydrogen adsorption to the edge and basal plane sites of MoSe<sub>2</sub> and WSe<sub>2</sub>.<sup>79</sup> They confirmed that the edges sites of MoSe<sub>2</sub> and WSe<sub>2</sub> were HER active with comparable or possibly higher activity than MoS<sub>2</sub> and WS<sub>2</sub>. Among the four compounds, the authors predicted MoSe<sub>2</sub> to be the most electrocatalytic active, followed closely by WS<sub>2</sub> since they had the most thermoneutral  $\Delta G_H$  for both metal and chalcogen edges. Using a similar growth process reported by the same group earlier as described in reference 62, Cui *et al.* synthesized MoSe<sub>2</sub> and WSe<sub>2</sub> films with vertically aligned edges through the rapid selenization of Mo or W films on various substrates, flat or curved.<sup>62, 80</sup> Both materials deposited on carbon fiber paper exhibited decent HER performance with a cathodic current density of 10 mA/cm<sup>2</sup> reached at  $\eta = 250$  mV and 300 mV for MoSe<sub>2</sub> and WSe<sub>2</sub>, respectively. No activity degradation was observed after 15000 continuous potential cycles.

At the end of this subsection, we want to add that a few non-layered transition metal chalcogenides, such as  $\text{CoS}_2$ ,  $\text{CoSe}_2$ ,  $\text{NiS}_2$  and  $\text{NiSe}_2$  are also potential candidates for HER even though they do not attract as much focus as  $\text{MoS}_2$  and its analogues.<sup>81-85</sup>

### 3.4 Transition metal carbides

There is also considerable interest in the development of early transition metal carbides (Group IV-VI), particularly tungsten or molybdenum carbides, as low-cost alternatives for HER electrocatalysis.<sup>86</sup> DFT calculations have suggested that the hybridization between metal and carbon orbitals gives rise to higher electron density of states at the Fermi level and a broad unoccupied d-band, affording characteristics resembling those of the Pt metal.<sup>87, 88</sup> As a result, early transition metal carbides often exhibit Pt-like electrocatalytic activity not only for HER, but also for the oxidation of hydrogen and small organic molecules such as methanol and formic acid.<sup>89, 90</sup> In addition, it is worth noting that they are not as vulnerable as Pt to poisoning and deactivation.

Since the first report by Trasatti *et al.* in 1964,<sup>91</sup> tungsten carbides (including WC and  $\text{W}_2\text{C}$ ) have been extensively studied as promising HER electrocatalysts. Their preparation typically involves the high-temperature reduction of metal precursors with carbonaceous gases (*e.g.*  $\text{CH}_4$ ,  $\text{C}_2\text{H}_6$  and CO) or other carbon-containing compounds.<sup>86</sup> One general problem associated with the high reaction temperature in the preparation of carbide nanomaterials is that it usually induces uncontrollable particle sintering, giving rise to particles with exceedingly low surface areas that are not suitable for commercial applications. A few solutions have been advanced. Takanabe *et al.* synthesized tungsten carbide nanocrystals through the reaction of tungsten precursors with mesoporous graphitic  $\text{C}_3\text{N}_4$  as the reactive template under inert gas at high temperatures.<sup>92</sup> By adjusting the precursor ratio and reaction temperature, the authors achieved a good control over the composition and structure of the final products. It was observed that WC synthesized at 1223 K exhibited the optimal HER performance over a wide range of pHs. This material was capable of sustaining the figure-of-merit

current density at a small overpotential of 125 mV, by far smaller than other tungsten carbide electrocatalysts available in literature. Its exchange current density was estimated to be  $0.35 \text{ mA/cm}^2$ , close to that of Pt ( $j_0 \approx 1 \text{ mA/cm}^2$ ) in 0.5 M H<sub>2</sub>SO<sub>4</sub>. Recently, Román-Leshkov *et al.* proposed a removable ceramic coating method to prepare non-sintered, ultrasmall transition metal carbides.<sup>93</sup> The essence of this method was to use SiO<sub>2</sub> coating to encapsulate nanoparticles of metal precursors and to prevent their sintering during the high- temperature carburization. Using this method, 1~2 nm WC nanoparticles supported on carbon were prepared with high electrocatalytic activities of ~100 times higher than commercial WC and within an order of magnitude of Pt for both HER and methanol oxidation reaction.

Molybdenum carbides are known to have more stoichiometries and phases. Among them, attention has been primarily focused on hexagonal  $\beta$ -Mo<sub>2</sub>C for its high HER performance. Leonard *et al.* synthesized molybdenum carbide nanomaterials of four different phases ( $\alpha$ -MoC<sub>1-x</sub>,  $\beta$ -Mo<sub>2</sub>C,  $\eta$ -MoC and  $\gamma$ -MoC) from the pyrolysis of a unique amine-metal oxide composite, and evaluated their HER performance in 0.1 M HClO<sub>4</sub>.<sup>94</sup> It was concluded that  $\beta$ -Mo<sub>2</sub>C had the highest activity with an exchange current density  $j_0 = 17.29 \mu\text{A/cm}^2$ , followed by  $\gamma$ -MoC ( $j_0 = 3.2 \mu\text{A/cm}^2$ ), whereas the other two phases were much less active. In a similar approach, Liu *et al.* prepared nanoporous Mo<sub>2</sub>C nanowires from templating molybdate/aniline hybrid nanowires (Figure 8).<sup>95</sup> The final Mo<sub>2</sub>C nanowires were composed of individual nanocrystallites of 10-15 nm hierarchically interconnected but free of aggregation, forming enriched nanoporosity and large surface areas (Figure 8A-C). Such an advantageous microstructure resulted in enhanced HER performance. In 0.5 M H<sub>2</sub>SO<sub>4</sub>, nanoporous Mo<sub>2</sub>C nanowires delivered a substantial current density of ~60 mA/cm<sup>2</sup> at an overpotential of 200 mV, and exhibited a Tafel slope of 53 mV/decade (Figure 8D). It also demonstrated robust short-term and long-term durability (Figure 8E).

Growing carbide nanomaterials on conductive carbon supports has also been proven an effective strategy. The carbon supports can improve the dispersion and electric conductivity of carbide

electrocatalysts, and hence promote their electrocatalytic performance. Adzic *et al.* used in-situ carburization of ammonium molybdate on carbon nanotubes (CNTs) and XC-72R carbon black to prepare supported  $\beta$ -Mo<sub>2</sub>C nanoparticles.<sup>96</sup> They demonstrated that growing Mo<sub>2</sub>C on a carbon support imparted a significant enhancement in the exchange current density and a remarkable reduction in the charge-transfer resistance. This synergistic effect was more obvious with carbon nanotube support. Its exchange current density reached  $1.4 \times 10^{-2}$  mA/cm<sup>2</sup> in 0.1 M HClO<sub>4</sub>. An HER current density of 10 mA/cm<sup>2</sup> was delivered at  $\eta = 152$  mV. Yang *et al.* prepared carbon layer stabilized Mo<sub>2</sub>C nanoparticles on reduced graphene oxide (RGO) nanosheets by a two-step method.<sup>97</sup> Owing to the excellent electrical coupling and large surface area of the graphene support, the hybrid electrocatalyst presented excellent activity and stability with an HER onset overpotential of ~70 mV and Tafel slope of ~57 mV/decade. Lee *et al.* applied a modified urea-glass route to disperse ~10 nm Mo<sub>2</sub>C nanoparticles on carbon nanotube-graphene (CNT-GR) support.<sup>98</sup> The large-area CNT-GR support was believed to greatly benefit the electron transfer during electrocatalysis and suppress the aggregation of Mo<sub>2</sub>C nanoparticles. Resulting Mo<sub>2</sub>C/CNT-GR hybrid showed a small onset overpotential of 62 mV and Tafel slope of 58 mV/decade, accompanied with excellent stability in acid media.

### 3.5 Transition metal nitrides

Like carbides, the formation of early transition metal nitrides modifies the nature of the d band of the parent metals, giving rise to catalytic properties that are distinct from the parent metals but similar to those of group VIII precious metals.<sup>86, 88</sup> Transition metal nitrides are usually prepared by nitridation of corresponding metal precursors with pure NH<sub>3</sub> or a mixture of NH<sub>3</sub> and inert gas at high temperatures. Molybdenum nitrides and their derivatives are among the most common materials examined for HER electrocatalysis under this category.

Depending on the starting precursors and nitriding temperature, molybdenum nitrides of different stoichiometries can form, *i.e.* MoN, Mo<sub>2</sub>N and Mo<sub>2</sub>N<sub>0.78</sub>.<sup>99, 100</sup> All are HER active. Xie *et al.* fabricated atomically thin MoN nanosheets by liquid exfoliation of the bulk material in N-methyl-2-pyrrolidone.<sup>101</sup> DFT calculations suggested that these exfoliated nanosheets were metallic and had higher charge density than the bulk counterpart. Their enriched density of active sites and metallic behaviour were believed to greatly facilitate the charge transfer and enhance the HER performance. Electrochemical measurements showed that MoN nanosheets exhibited a low onset overpotential of 100 mV and a Tafel slope of 90 mV/decade. The cathodic current density at η = 300 mV reached 38.5 mA/cm<sup>2</sup>, about 35 fold larger compared to that of the bulk counterpart. This underscores the great structural advantages of atomically thin nanosheets in electrocatalysis. Muckerman *et.al* reported the preparation of carbon black supported Mo<sub>2</sub>N nanoparticles by annealing a mixture of MoO<sub>3</sub> powder and the Vulcan XC-72R carbon black in a NH<sub>3</sub>-purged tube furnace at 700°C.<sup>102</sup> The average grain size of Mo<sub>2</sub>N nanoparticles was 8.5 nm estimated from XRD. Mo<sub>2</sub>N/carbon black hybrid displayed decent HER activity in 0.1 M HClO<sub>4</sub>. Its onset overpotential and overpotential to reach 10 mA/cm<sup>2</sup> were ~150 mV and 300 mV, respectively.

The HER performance of molybdenum nitrides can be further promoted with the introduction of a late transition metal such as Ni or Co. For example, Sasaki *et al.* prepared nickel-molybdenum nitride nanosheets on a carbon support (NiMoN<sub>x</sub>/C) as a highly active HER electrocatalyst (Figure 9).<sup>103</sup> The synthesis consisted of two steps: first the reduction of a carbon supported ammonium molybdate and nickel nitrate mixture with H<sub>2</sub> at 400°C to form NiMo metal nanoparticles, and subsequently ammonolysis at 700°C which transformed NiMo nanoparticles to NiMoN<sub>x</sub> nanosheets about 4-15 nm thick (Figure 9A,B). Resulting NiMoN<sub>x</sub>/C demonstrated better corrosion resistance compared to NiMo in acidic medium. Its exchange current density for HER was 0.24 mA/cm<sup>2</sup>, roughly one third that of the Pt/C benchmark (0.78 mA/cm<sup>2</sup>), and about an order of magnitude higher than those of MoN/C (0.036 mA/cm<sup>2</sup>) and NiMo alloys. It also featured a reduced onset

overpotential of 78 mV/decade, and a small Tafel slope of 35.9 mV/decade indicative of the recombination reaction as the possible rate determining step during HER (Figure 9C,D). Along the same line, Khalifah *et al.* studied the promoting effect of Co on the HER performance of molybdenum nitride.<sup>104</sup> Nanostructured  $\text{Co}_{0.6}\text{Mo}_{1.4}\text{N}_2$  was made by a two-step solid state reaction. The compound was comprised of alternating close-packed layers of transition metals in octahedral and trigonal prismatic coordination. Neutral powder diffraction revealed that the octahedral sites contained a mixture of divalent Co and trivalent Mo, and the trigonal prismatic sites contained Mo in a higher oxidation state. It was believed that such a layered structure allowed Co to tune the electronic states of Mo at the catalyst surface, leading to better HER activity.  $\text{Co}_{0.6}\text{Mo}_{1.4}\text{N}_2$  requires an overpotential of  $\sim 200$  mV to reach  $10 \text{ mA/cm}^2$ , while for MoN the overpotential almost doubled in order to drive the same current density.

### 3.6 Transition metal borides

Transition metal borides have been investigated for HER electrocatalysis since more than four decades ago. In 1974, Kuznetsova *et al.* studied the HER kinetics on some transition metals in 1 M  $\text{H}_2\text{SO}_4$  and found their electrocatalytic activity increased in the order  $\text{ZrB}_2 < \text{NbB}_2 < \text{TaB}_2 < \text{W}_2\text{B}_5$ .<sup>105</sup> In 1990s, focus was mainly placed on nickel boride – usually amorphous – as the potential HER electrocatalyst for alkaline electrolyzers.<sup>106-109</sup> This compound was well comparable to Raney Ni in activity with improved corrosion resistance. More recent researches have explored other candidates. Hu *et al.* evaluated the HER activity of commercially available tetragonal  $\alpha$ -MoB microparticles in both acidic (1 M  $\text{H}_2\text{SO}_4$ ) and alkaline (1 M KOH) electrolytes.<sup>110</sup> The material was slightly more active in acid than in base, but its electrocatalytic characteristics were overall similar: Tafel slopes of 55-59 mV/decade and exchange current densities of  $1.4\text{-}2.0 \mu\text{A/cm}^2$  were measured; and the overpotentials to sustain a current density of  $20 \text{ mA/cm}^2$  were 225-240 mV. Nevertheless, MoB

presented drastically different durability behaviours in these two electrolytes. It was indefinitely stable in 1 M H<sub>2</sub>SO<sub>4</sub>, while in 1 M KOH it became corroded after just one hour.

### 3.7 Transition metal phosphides

Transition metal phosphides have been traditionally studied as catalysts for hydrogenation, especially for hydrodesulfurization.<sup>111, 112</sup> It is only since 2013 that phosphides have attracted widespread interest for HER electrocatalysis. Now they are among the most active non-precious metal based HER electrocatalysts available so forth. The most common approach to prepare phosphide materials involves the reduction of phosphate at elevated temperatures.<sup>112</sup> Development of new methods facilitating the control of phase composition, structure, morphology and dispersion of phosphide electrocatalysts so as to achieve optimal HER performance is an active area of ongoing research.

Schaak *et al.* first employed tri-n-octylphosphine (TOP) as the phosphorus precursor in the preparation of Ni<sub>2</sub>P and CoP nanoparticles through high-temperature solution phase reaction (Figure 10).<sup>113, 114</sup> The decomposition of TOP at ~320°C liberated phosphorus, which then reacted with pre-formed metal nanoparticles via a nanoscale Kirkendall pathway, forming hollow crystalline phosphide nanoparticles with uniform sizes (10-20 nm, Figure 10A,B,E,F). When loaded on Ti foil substrates, these nanoparticles showed excellent HER performance in 0.5 M H<sub>2</sub>SO<sub>4</sub>. Between the two, CoP was more active than Ni<sub>2</sub>P. The overpotential required to reach a cathodic current density of 20 mA/cm<sup>2</sup> was 85 mV and 130 mV for CoP and Ni<sub>2</sub>P, respectively (Figure 10C,G). The TOF at  $\eta = 100$  mV on CoP ( $0.046\text{ s}^{-1}$ ) was calculated to be about 3 times higher than on Ni<sub>2</sub>P ( $0.015\text{ s}^{-1}$ ). Both Ni<sub>2</sub>P and CoP electrocatalysts demonstrated decent operation durability in acid, but their stability in base was rather poor. In 1 M KOH, Ni<sub>2</sub>P nanoparticles were found to quickly degrade to Ni, resulting in a significant loss of HER activity. Later, the authors applied the same method to the preparation of 3~4 nm amorphous MoP and WP nanoparticles.<sup>115, 116</sup> It is important to note that these two

compounds have higher crystallization temperatures ( $>600^{\circ}\text{C}$ ) than the phosphides of late transition metals, so only amorphous nanoparticles were produced from the high-temperature solution phase reaction. Both materials displayed great HER activity and durability in acid with  $10 \text{ mA/cm}^2$  achieved at  $\eta = 90$  and  $120 \text{ mV}$  for MoP and WP, respectively.

Using TOP as the phosphorus precursor affords a great control over the product morphology. Unfortunately, its pitfall is similarly obvious: organic phosphine is highly toxic and expensive. It is not amenable to the large scale production of phosphide catalysts. An alternative phosphorus precursor that has been frequently utilized is hypophosphite. When mildly heated, hypophosphite decomposes and releases gaseous  $\text{PH}_3$  for further reaction with metal precursors to yield corresponding metal phosphides. Following this approach, Hu *et al.* synthesized polydispersed  $\text{Ni}_2\text{P}$  nanoparticles of 10-100 nm in size.<sup>117</sup> The electrocatalyst showed comparable HER performance to the  $\text{Ni}_2\text{P}$  nanoparticles reported by Schaak *et al.* in the acidic electrolyte, but exhibited much improved durability in the alkaline electrolyte probably due to its slower corrosion rate associated with larger particle sizes. In another report, CoP nanowires, nanosheets and nanoparticles were prepared by Sun *et al.* via the low-temperature ( $\sim 300^{\circ}\text{C}$ ) phosphidation of nanostructured cobalt oxide or hydroxide templates with morphologies preserved.<sup>118</sup> Among them, CoP nanowires were measured to be the most active. Its Tafel slope and overpotential needed to drive  $10 \text{ mA/cm}^2$  were  $54 \text{ mV/decade}$  and  $110 \text{ mV}$ , respectively. In their follow-up studies, the authors made further improvements by successfully growing nanoporous CoP nanowire arrays on carbon cloth<sup>119</sup> and CoP nanoparticles on carbon nanotubes.<sup>120</sup> In particular, the CoP nanowire array electrode only needed overpotentials of 67, 100 and  $204 \text{ mV}$  to drive current densities of 10, 20 and  $100 \text{ mA/cm}^2$  respectively in  $0.5 \text{ M H}_2\text{SO}_4$ , succeeding the activities of most non-precious metal based HER electrocatalysts in acidic electrolyte.<sup>119</sup> It was worth mentioning that the electrocatalyst also presented good activity and durability in neutral and alkaline electrolytes. Furthermore, this

low-temperature phosphidation method was extended to the preparation of FeP and Cu<sub>3</sub>P nanowire arrays with great HER performance by the same group.<sup>121-123</sup>

As mentioned above, MoP and WP have higher crystallization temperature. As a result, high-temperature phosphidation is necessary to achieve their crystalline products. Wang *et al.* reported that crystalline Mo<sub>3</sub>P and MoP powders were prepared by reacting stoichiometric amounts of ammonium molybdate and (NH<sub>4</sub>)HPO<sub>4</sub> at 650°C and 800°C, respectively.<sup>124</sup> Electrochemical measurements demonstrated that MoP was highly HER active with an onset overpotential of 50 mV, a Tafel slope of 54 mV/decade and a HER current density of 30 mA/cm<sup>2</sup> at  $\eta = 180$  mV, whereas Mo<sub>3</sub>P exhibited significantly inferior performance. The remarkable HER activity of MoP was suggested to stem from P terminated surface, which had a suitable  $\Delta G_H$  from DFT calculations. To mitigate MoP particle sintering during the high-temperature phosphidation, citric acid was introduced as the chelating agent by Sun *et al.*<sup>125</sup> After the reaction, a closely interconnected network of MoP nanoparticles was formed. It was measured to have a BET surface area of 143.3 m<sup>2</sup>/g, more than three times higher than that of MoP nanoparticles prepared without citric acid. Such a large gain in specific surface area translated to a dramatic enhancement in HER activity. The cathodic current densities at  $\eta = 200$  mV were reported to be 100 mA/cm<sup>2</sup> and 1.7 mA/cm<sup>2</sup> for MoP nanoparticles prepared with and without citric acid, respectively. In a very recent study, Jaramillo *et al.* discovered that the HER performance of MoP could be further promoted by a post-sulfidation treatment in an H<sub>2</sub>S atmosphere, creating surface phosphosulfides with bulk crystal structure preserved.<sup>126</sup> This post-sulfidation reduced the overpotential required to reach 10 mA/cm<sup>2</sup> from 117 mV (for MoP) to 86 mV (for MoP|S). Sun *et al.* demonstrated red phosphorus could also be used as the precursor for phosphidation.<sup>127</sup> At 800°C, its vapor reacted with WO<sub>3</sub> nanowire arrays grown on carbon cloth and transformed it to WP nanowire arrays. Resulting carbon cloth electrode exhibited great HER activity and durability in electrolytes of all pHs.

### 3.8 Metal free catalysts

Carbon-based electrocatalysts free of metals are also the focus of recent research. However, pristine carbon materials are electrochemically inert. This is the basis why we can use many carbon-based current collectors such as glassy carbon, carbon paper and carbon cloth in electrochemical experiments. Chemical modification of the carbon surface, *e.g.* heteroatom doping, is usually necessary in order to enhance its electrocatalytic activity via forming heteroatom functionalities.<sup>128</sup>

Occasionally, there are studies claiming that “metal-free” carbon nanotubes are electrocatalytically active. For example, Sun *et al.* reported that oxidization of carbon nanotubes introduced abundant carboxylic groups to their surface, which in turn made nanotubes highly active and durable for HER in acid.<sup>129</sup> The electrocatalyst showed an onset overpotential of 100 mV and required an overpotential of 220 mV to reach 10 mA/cm<sup>2</sup>. While the HER activity reported in this work is certainly adorable, it may be mainly attributed to metal impurities (*e.g.* Fe, Co, Ni and Mo, usually 1~10 wt%) in nanotubes that are commonly employed as the catalyst seeds for carbon nanotube growth. These impurities may exist in the forms of metals, oxides or carbides. We recently demonstrated that it was not possible to completely eliminate these impurities, even after rigorous purification.<sup>130, 131</sup> Depending on their concentration, they may not be readily detected via regular techniques such as x-ray photoelectron spectroscopy, but may still significantly contribute to the electrocatalytic activity.<sup>132-134</sup>

Heteroatom doped graphene nanosheets have recently been explored as metal-free HER electrocatalysts. Using DFT calculations, Qiao *et al.* explored several heteroatom (N, B, O, S, P and F) doped or co-doped graphene models and predicted that N and P codoping afforded the optimal HER activity with  $|\Delta G_H| \sim 0.08$  eV.<sup>135</sup> To experimentally corroborate this prediction, the authors prepared N and P co-doped graphene by annealing chemically exfoliated graphene oxide powder with a melamine and triphenylphosphine mixture at 950°C in Ar atmosphere. The final product was

found to contain 4.6 at% of N and 1.63 at% of P. Electrochemical measurements showed that this material was indeed more active than pristine and all the singly doped graphene. It had a Tafel slope of 91 mV/decade and required an overpotential of 420 mV to drive 10 mA/cm<sup>2</sup> in 0.5 M H<sub>2</sub>SO<sub>4</sub>. In a parallel study, Chen *et al.* synthesized N and S co-doped nanoporous graphene by chemical vapor deposition on Ni substrate using pyridine and thiophene as the nitrogen and sulfur precursors.<sup>136</sup> The best co-doped material exhibited an HER onset overpotential of 130 mV and a Tafel slope of 80.5 mV/decade in acid. The overpotential required to deliver 10 mA/cm<sup>2</sup> was 280 mV. Based on DFT calculations, the authors proposed that the synergistic coupling of S and N dopants with geometric defects in the graphene lattice reduced |ΔG<sub>H</sub>| on graphene, and hence was responsible for the improved HER activity. Here, we notice the large inconsistency in the HER activity of two aforementioned co-doped graphene materials, and speculate that it is probably caused by the Ni contamination in Chen's study. Even though the authors stated that the residual Ni was less than 0.07 at%, such a trace amount of Ni might still promote the HER activity of S and N co-doped graphene to certain extent.

Carbon nitride (C<sub>3</sub>N<sub>4</sub>) with similar two-dimensional crystal structure is another metal-free candidate that has attracted considerable interest for electrocatalysis. It is typically synthesized by the thermal condensation of organic molecules containing nitrogen and carbon atoms, *e.g.* cyanamide and melamine. Shalom *et al.* used hydrogen-bonded cyanuric acid melamine supermolecular complex as the precursor to form ordered C<sub>3</sub>N<sub>4</sub> nanorod arrays on different substrates.<sup>137</sup> The nanorod growth was directed by the interactions between the hydroxyl and amine groups of the complex precursor and the surface of the substrate. C<sub>3</sub>N<sub>4</sub> nanorods grown on FTO electrode demonstrated decent HER activity with onset overpotentials of ~100 mV and ~250 mV in alkaline and neutral media, respectively. However, their current densities were rather poor. Further improvement on the HER activity of C<sub>3</sub>N<sub>4</sub> has been made by hybridizing it with graphene. For example, C<sub>3</sub>N<sub>4</sub> grown on N-doped graphene nanosheets (C<sub>3</sub>N<sub>4</sub>@NG) was demonstrated as an

efficient HER electrocatalyst by Qiao *et al.*<sup>138</sup> The hybrid was prepared via annealing a mixture of graphene oxide and dicyandiamide. During the heat treatment, graphene oxide was simultaneously reduced and doped with N by gaseous NH<sub>3</sub> released from the condensation of dicyandiamide. In 0.5 M H<sub>2</sub>SO<sub>4</sub>, C<sub>3</sub>N<sub>4</sub>@NG was shown to deliver a HER current density of 10 mA/cm<sup>2</sup> at η ~ 240 mV with a good cycling durability, comparable to many metal based electrocatalysts (Figure 11A,B). DFT calculations revealed that this impressive electrocatalytic activity was originated from the chemical coupling of the two components within the hybrid nanostructure: C<sub>3</sub>N<sub>4</sub> provided highly active hydrogen adsorption sites, while N-graphene facilitated the electron-transfer process for the proton reduction. Such a synergistic effect resulted in a favorable adsorption-desorption behavior with |ΔG<sub>H</sub>| close to zero (Figure 11C). Along the same line, Qu *et al.* assembled C<sub>3</sub>N<sub>4</sub> nanoribbons on graphene nanosheets to form three dimensional interconnected networks by a hydrothermal method.<sup>139</sup> This hybrid material displayed a similar overpotential value of 207 mV to achieve 10 mA/cm<sup>2</sup> and a Tafel slope of 54 mV/decade.

#### 4. Conclusion and Perspective

In this article, we have reviewed the recent developments of HER electrocatalysts, from precious metals to non-precious metal compounds and finally to metal-free materials. Figure 12 summarizes and compares HER activities of these electrocatalysts in terms of overpotential needed to reach  $j = 10$  mA/cm<sup>2</sup> in acidic or alkaline electrolytes. Please note that since  $j$  represents the geometric current density, the graphic data here reflect not the intrinsic activity but rather the apparent activity of different HER electrocatalysts reviewed in this article. It is not feasible for us to compare their intrinsic activities given the variety of their compositions and microstructures. In the time being, platinum group metals remain the most active HER electrocatalysts. However, significant advances have been made on the other candidates in the past 5 years, which substantially narrow their gap from the precious metal benchmarks. Among them, Ni-based alloys (*e.g.* NiMo) are probably the

most efficient HER electrocatalysts in alkaline electrolytes, and metal phosphides – in spite of their relatively short history of research – lead in activity for HER in acids. Even though these electrocatalysts are still unable to rival PGMs on site-specific activities, they hold great promises as low-cost alternatives for practical applications which frequently demand a trade-off between activity and cost.

There are several challenges toward the future development of HER electrocatalysts. First, their activities have to be further promoted. For practical applications, it is desired that non-precious metal based electrocatalysts have an onset overpotential within 100 mV and overpotential at  $j = 10 \text{ mA/cm}^2$  within 150 mV. At present, only phosphides in acids and metal alloys in bases can meet this activity criterion (Figure 12). More importantly, most new electrocatalysts under current development are for acidic electrolytes. Their performance in alkaline electrolytes is significantly worse owing to the inefficient dissociation of water to initiate the Volmer reaction in alkaline environment.<sup>113</sup> This poses a potential problem when HER is coupled with oxygen evolution reaction (OER) in the overall water splitting since all OER electrocatalysts available at present only function in alkaline or neutral condition.<sup>140, 141</sup> Second, their stabilities need more improvements. HER electrocatalysts are usually oxidation-sensitive. Transition metal chalcogenides, carbides, nitrides, borides and phosphides are all prone to gradual oxidation when exposed to air or aerated solution, forming inert surface oxide layers. This is even more severe in alkaline media. For example, the HER activity of MoS<sub>2</sub> in alkaline electrolytes usually deteriorate in just a few cycles. In addition, activity and stability are sometimes anti-correlated, i.e. the most active electrocatalysts are usually not very stable. It can be understood through the general observation that as the particle size of one electrocatalyst decreases, both of its HER activity and corrosion rate increase. Strategies are called for to stabilize the electrode-electrolyte interface to enable prolonged operation on the scale of not hours, but weeks or months. Third, the preparation methods have to be

economical and green. The most applicable approach should carefully avoid expensive precursors, toxic or corrosive reagents, high-temperature, high-pressure or low-pressure reaction conditions, and with no or low hazardous byproducts.

From our review, a few general keys can be identified and summarized to assist in the future design of HER electrocatalysts.

*Nanostructure engineering.* With the advent of nanotechnology, the prospects for using nanomaterials with atomically tailored structures in electrocatalysis have progressed rapidly. Nanostructuring now is the most common tactic employed today to promote the activity of catalysts. When the size of materials is reduced from macroscale to nanoscale, their electrochemically active surface areas increase dramatically, resulting in heightened activities. Nanostructuring may also introduce structural defects or disorders, which could strongly influence local electronic structure and serve as catalytically active sites for electrochemical reactions. In the future, the most successful HER electrocatalysts may not necessarily have well-defined morphologies such as nanoparticles, nanowires and nanosheets, but they are very likely to possess porous structures at the nanoscale with large electrochemically accessible surface areas for fast charge transfer reaction on the surface.

*Hybrid structures.* Electrocatalysis relies on electricity to drive catalytic reactions. Unfortunately, most electrocatalysts are bad electric conductors. Even though this problem can be alleviated by mixing with conductive additives, it still constrains their electrocatalytic performance, especially under large current densities ( $>10\text{ mA/cm}^2$ ). Recently, it is found that integrating electrocatalysts with conductive carbon supports such as graphene, carbon nanotubes or carbon fibers presents a feasible solution to this challenge. A good carbon support material can greatly facilitate the electron transport to and from electrocatalysts, and improve their dispersion. Synergistic coupling between the carbon support and electrocatalyst materials may also give rise to unexpected gain in activity and durability. One example is

$\text{MoS}_2$  and graphene hybrid electrocatalyst developed by us in 2011.<sup>63</sup> This material features nanoscopic few-layer  $\text{MoS}_2$  structures with abundant edges uniformly dispersed on graphene sheets. When evaluated for HER, it exhibits small onset overpotential of  $\sim 100$  mV and Tafel slope of 40 mV/decade, significantly improved over free  $\text{MoS}_2$  particles or graphene alone. Following this early work, a number of studies have explored the effect of hybrid structures for electrocatalysis, all with positive outcomes.<sup>84, 97, 142, 143</sup> In the future, if the production costs of graphene or carbon nanotubes can be lowered through economies of scales, we believe there is no other conceivable barrier against the practical implementation of hybrid electrocatalysts.

*Proper crystal structures and crystallinity.* Crystal structure and crystallinity of electrocatalyst materials usually have large impacts on their performance, but are often overlooked. Some compounds have several polymorphs with very different electrochemical properties. For example, layered transition metal dichalcogenides  $\text{MX}_2$  have hexagonal 2H structure and tetragonal 1T structure. Experiments reveal that the latter is more electric conductive than the former, and exhibits substantially higher electrocatalytic activity.<sup>64-66, 75, 77</sup> In light of this, recent efforts have been directed toward achieving and stabilizing 1T structure for HER. On the other hand, increasing evidence suggests that amorphous materials may have unique advantages in electrocatalysis. The absence of long-range order is detrimental to their electronic and photonic properties, but for electrocatalytic applications, it creates abundant coordinatively unsaturated sites on the surface as the catalytic centers.<sup>69, 70</sup> In the design of future electrocatalysts, attention should be given to the proper selection of crystal structure and crystallinity for optimal electrocatalytic performance.

*Proper doping or alloying.* Doping or alloying with foreign atoms is an effective way to tune materials' electronic structure, which in turn affect their interaction with hydrogen intermediates and ultimately electrocatalytic activities. There are many examples of successful doping of HER electrocatalysts: incorporation of Co or Ni in  $\text{MoS}_2$  is reported to reduce  $\Delta G_{\text{H}}$  on S-edges of  $\text{MoS}_2$ , and hence promote its HER activities;<sup>73</sup> we recently demonstrate that  $\text{MoS}_{2(1-x)}\text{Se}_{2x}$

alloys exhibit improved performance in comparison to either MoS<sub>2</sub> or MoSe<sub>2</sub> as a result of their optimal ΔG<sub>H</sub>;<sup>74</sup> similarly, heteroatom (N, B, P and so on) doping of normally inert carbon materials renders them with very decent electrocatalytic performance.<sup>135, 144</sup> For new HER electrocatalysts, the selection of proper dopant types, doping level or alloying composition can probably be guided by DFT-based computational tools.

*Learning from HDS reactions.* In the search for new HER electrocatalysts, we can borrow knowledge from traditional hydrotreating catalysts (HDT). This is because HDT also involves hydrogen adsorption as the intermediate step. As a result, HDT and HER share similar requirements on the hydrogen binding energy on catalyst surfaces.<sup>15</sup> In 1981, Chianelli *et al.* reported that HDT activities of transition metal sulfides were related to the position metals occupy in the periodic table as shown in Figure 13.<sup>51</sup> MoS<sub>2</sub>, WS<sub>2</sub> and Co<sub>9</sub>S<sub>8</sub> established as the most active non-precious metal sulfide HDT catalysts at that time have all been identified as excellent HER electrocatalysts recently. From Figure 13, it is also worth noting that the HDT activity of Cr<sub>2</sub>S<sub>3</sub> is just below MoS<sub>2</sub>, and based on the above rationale, we can reasonably expect Cr<sub>2</sub>S<sub>3</sub> to have good HER activity. The growing correlation between these two catalytic reactions points to a new avenue for further expanding the search for high-performance HER electrocatalysts.

## Author Biographies



*Min Zeng received his bachelor's degree in Materials Science and Engineering from Soochow University, China in 2007. He then completed his master's degree in Electrochemistry from Jiangsu Normal University in 2010 and his Ph.D. degree in Condensed Matter Physics from the Institute of Physics, University of Chinese Academy of Sciences in 2014. Now he works as a postdoctoral researcher under the supervision of Prof. Yanguang Li in the Institute of Functional Nano & Soft Materials (FUNSOM) at Soochow University. His current research focuses on developing nanostructured functional materials for electrocatalysis.*



*Yanguang Li is a Professor in the Institute of Functional Nano & Soft Materials (FUNSOM) and College of Nano Science & Technology (CNST) at Soochow University, China. He received his BS in Chemistry from Fudan University, China in 2005; and obtained his PhD in Chemistry from Ohio State University in 2010. He then moved to the Stanford University and completed a post-doctoral training before taking the current faculty position in 2013. His research focuses on nanostructured functional materials for energy applications, particularly in the realm of electrocatalysis, advanced batteries and photo water splitting.*

## Acknowledgements

We acknowledge supports from the National Natural Science Foundation of China (51472173), the National Natural Science Foundation of Jiangsu Province (BK20140302), Jiangsu Key Laboratory for Carbon-Based Functional Materials and Devices, the Priority Academic Program Development of

Jiangsu Higher Education Institutions and Collaborative Innovation Center of Suzhou Nano Science and Technology.

## References

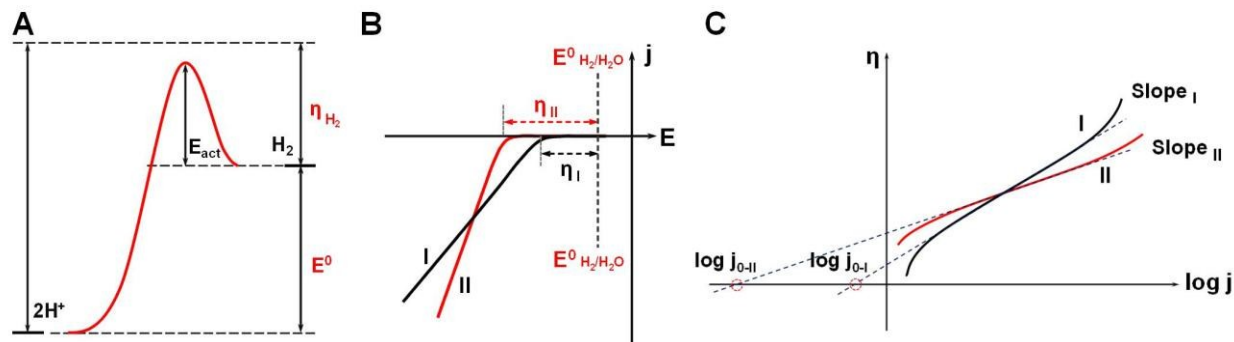
1. J. O. M. Bockris, *Int. J. Hydrogen Energy*, 2002, **27**, 731-740.
2. M. S. Dresselhaus and I. L. Thomas, *Nature*, 2001, **414**, 332-337.
3. J. A. Turner, *Science*, 2004, **305**, 972-974.
4. N. S. Lewis and D. G. Nocera, *Proc. Natl. Acad. Sci. USA*, 2006, **103**, 15729-15735.
5. M. G. Walter, E. L. Warren, J. R. McKone, S. W. Boettcher, Q. Mi, E. A. Santori and N. S. Lewis, *Chem. Rev.*, 2010, **110**, 6446-6473.
6. J. R. Rostrup-Nielsen, *Catal. Rev. Sci. Eng.*, 2004, **46**, 247-270.
7. J. C. Fontecilla-Camps, A. Volbeda, C. Cavazza and Y. Nicolet, *Chem. Rev.*, 2007, **107**, 4273-4303.
8. V. S. Thoi, Y. Sun, J. R. Long and C. J. Chang, *Chem. Soc. Rev.*, 2013, **42**, 2388-2400.
9. J. R. McKone, S. C. Marinescu, B. S. Brunschwig, J. R. Winkler and H. B. Gray, *Chem. Sci.*, 2014, **5**, 865-878.
10. W. Kreuter and H. Hofmann, *Int. J. Hydrogen Energy*, 1998, **23**, 661-666.
11. D. M. F. Santos and C. A. C. Sequeira, *Quim. Nova*, 2013, **36**, 1176-1193.
12. S. Trasatti, *J. Electroanal. Chem.*, 1972, **39**, 163-184.
13. I. A. Raj and K. I. Vasu, *J. Appl. Electrochem.*, 1990, **20**, 32-38.
14. D. E. Brown, M. N. Mahmood, M. C. M. Man and A. K. Turner, *Electrochim. Acta*, 1984, **29**, 1551-1556.
15. C. G. Morales-Guio, L. A. Stern and X. Hu, *Chem. Soc. Rev.*, 2014, **43**, 6555-6569.
16. Y. Li, *IEEE Nanotech. Mag.*, 2014, **8**, 22-28.
17. M. S. Faber and S. Jin, *Energy Environ. Sci.*, 2014, **7**, 3519-3542.
18. Y. Y. Liang, Y. G. Li, H. L. Wang and H. J. Dai, *J. Am. Chem. Soc.*, 2013, **136**, 2013-2036.
19. A. J. Bard and L. R. Faulkner, *Electrochemical Methods: Fundamentals and Applications*, John Wiley, New York, 2000.
20. G. Eliezer, *Physical Electrochemistry*, John Wiley, New York, 2011.
21. D. T. Sawyer, A. Sobkowiak and J. L. Roberts, *Electrochemistry for Chemists*, John Wiley, New York, 1995.
22. C. C. L. McCrory, S. H. Jung, J. C. Peters and T. F. Jaramillo, *J. Am. Chem. Soc.*, 2013, **135**, 16977-16987.
23. J. O. M. Bockris and E. C. Potter, *J. Electrochem. Soc.*, 1952, **99**, 169.
24. J. K. Norskov, T. Bligaard, A. Logadottir, J. R. Kitchin, J. G. Chen, S. Pandelov and J. K. Norskov, *J. Electrochem. Soc.*, 2005, **152**, J23-J26.
25. J. Greeley, T. F. Jaramillo, J. Bonde, I. B. Chorkendorff and J. K. Norskov, *Nat. Mater.*, 2006, **5**, 909-913.
26. P. Sabatier, *Ber. Deutschen Chem. Gesellschaft*, 1911, **44**, 1984-2001.
27. R. Parsons, *Trans. Faraday Soc.*, 1958, **54**, 1053-1063.
28. B. Hinnemann, P. G. Moses, J. Bonde, K. P. Jorgensen, J. H. Nielsen, S. Horch, I. Chorkendorff and J.

- K. Norskov, *J. Am. Chem. Soc.*, 2005, **127**, 5308-5309.
29. J. Chen, B. Lim, E. P. Lee and Y. Xia, *Nano Today*, 2009, **4**, 81-95.
30. Y. Xu and B. Zhang, *Chem. Soc. Rev.*, 2014, **43**, 2439-2450.
31. J. T. Zhang and C. M. Li, *Chem. Soc. Rev.*, 2012, **41**, 7016-7031.
32. D. V. Esposito and J. G. Chen, *Energ. Environ. Sci.*, 2011, **4**, 3900-3912.
33. D. V. Esposito, S. T. Hunt, A. L. Stottlemeyer, K. D. Dobson, B. E. McCandless, R. W. Birkmire and J. G. Chen, *Angew. Chem. Int. Ed.*, 2010, **49**, 9859-9862.
34. D. V. Esposito, S. T. Hunt, Y. C. Kimmel and J. G. Chen, *J. Am. Chem. Soc.*, 2012, **134**, 3025-3033.
35. T. G. Kelly, K. X. Lee and J. G. Chen, *J. Power Sources*, 2014, **271**, 76-81.
36. H. E. G. Rommal and P. J. Moran, *J. Electrochem. Soc.*, 1988, **135**, 343-346.
37. D. M. Soares, O. Teschke and I. Torriani, *J. Electrochem. Soc.*, 1992, **139**, 98-105.
38. K. Lohrberg and P. Kohl, *Electrochim. Acta*, 1984, **29**, 1557-1561.
39. P. Los, A. Rami and A. Lasia, *J. Appl. Electrochem.*, 1993, **23**, 135-140.
40. M. M. Jaksic, *Electrochim. Acta*, 2000, **45**, 4085-4099.
41. I. A. Raj and K. I. Vasu, *J. Appl. Electrochem.*, 1992, **22**, 471-477.
42. J. R. McKone, B. F. Sadtler, C. A. Werlang, N. S. Lewis and H. B. Gray, *ACS Catal.*, 2013, **3**, 166-169.
43. Y. H. Wang, G. X. Zhang, W. W. Xu, P. B. Wan, Z. Y. Lu, Y. P. Li and X. M. Sun, *Chemelectrochem*, 2014, **1**, 1138-1144.
44. R. Subbaraman, D. Tripkovic, D. Strmcnik, K. C. Chang, M. Uchimura, A. P. Paulikas, V. Stamenkovic and N. M. Markovic, *Science*, 2011, **334**, 1256-1260.
45. N. Danilovic, R. Subbaraman, D. Strmcnik, K. C. Chang, A. P. Paulikas, V. R. Stamenkovic and N. M. Markovic, *Angew. Chem. Int. Ed.*, 2012, **51**, 12495-12498.
46. M. Gong, W. Zhou, M. C. Tsai, J. G. Zhou, M. Y. Guan, M. C. Lin, B. Zhang, Y. F. Hu, D. Y. Wang, J. Yang, S. J. Pennycook, B. J. Hwang and H. J. Dai, *Nat. Commun.*, 2014, **5**.
47. M. Gong, Y. Li, H. Wang, Y. Liang, J. Z. Wu, J. Zhou, J. Wang, T. Regier, F. Wei and H. Dai, *J. Am. Chem. Soc.*, 2013, **135**, 8452-8455.
48. J. Deng, P. Ren, D. Deng and X. Bao, *Angew. Chem. Int. Ed.*, 2015, **54**, 2100-2104.
49. M. Tavakkoli, T. Kallio, O. Reynaud, A. G. Nasibulin, C. Johans, J. Sainio, H. Jiang, E. I. Kauppinen and K. Laasonen, *Angew. Chem. Int. Ed. Engl.*, 2015, **54**, 4535-4538.
50. J. R. Lince and P. D. Fleischauer, *J. Mater. Res.*, 1987, **2**, 827-838.
51. T. A. Pecoraro and R. R. Chianelli, *J. Catal.*, 1981, **67**, 430-445.
52. H. Tributsch and J. C. Bennett, *J. Electroanal. Chem.*, 1977, **81**, 97-111.
53. T. F. Jaramillo, K. P. Jorgensen, J. Bonde, J. H. Nielsen, S. Horch and I. Chorkendorff, *Science*, 2007, **317**, 100-102.
54. D. Merki and X. L. Hu, *Energ. Environ. Sci.*, 2011, **4**, 3878-3888.
55. A. B. Laursen, S. Kegnaes, S. Dahl and I. Chorkendorff, *Energ. Environ. Sci.*, 2012, **5**, 5577-5591.
56. Y. Yan, B. Y. Xia, Z. C. Xu and X. Wang, *ACS Catal.*, 2014, **4**, 1693-1705.
57. M. Chhowalla, H. S. Shin, G. Eda, L. J. Li, K. P. Loh and H. Zhang, *Nat. Chem.*, 2013, **5**, 263-275.
58. R. Tenne and M. Redlich, *Chem. Soc. Rev.*, 2010, **39**, 1423-1434.
59. L. Margulis, G. Salitra, R. Tenne and M. Talianker, *Nature*, 1993, **365**, 113-114.
60. J. Kibsgaard, Z. B. Chen, B. N. Reinecke and T. F. Jaramillo, *Nat. Mater.*, 2012, **11**, 963-969.
61. J. F. Xie, H. Zhang, S. Li, R. X. Wang, X. Sun, M. Zhou, J. F. Zhou, X. W. Lou and Y. Xie, *Adv. Mater.*, 2013, **25**, 5807-5813.

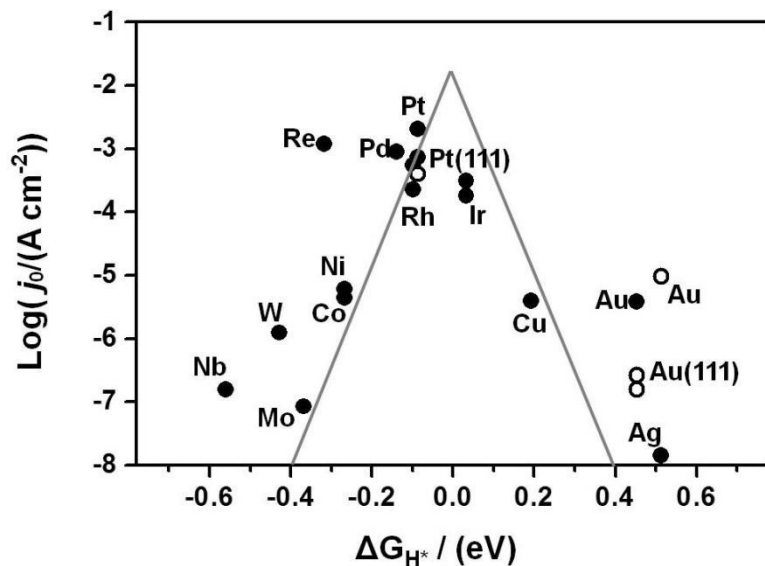
62. D. S. Kong, H. T. Wang, J. J. Cha, M. Pasta, K. J. Koski, J. Yao and Y. Cui, *Nano Lett.*, 2013, **13**, 1341-1347.
63. Y. G. Li, H. L. Wang, L. M. Xie, Y. Y. Liang, G. S. Hong and H. J. Dai, *J. Am. Chem. Soc.*, 2011, **133**, 7296-7299.
64. X. Huang, Z. Y. Zeng and H. Zhang, *Chem Soc Rev*, 2013, **42**, 1934-1946.
65. M. A. Lukowski, A. S. Daniel, F. Meng, A. Forticaux, L. S. Li and S. Jin, *J. Am. Chem. Soc.*, 2013, **135**, 10274-10277.
66. H. Wang, Z. Lu, S. Xu, D. Kong, J. J. Cha, G. Zheng, P.-C. Hsu, K. Yan, D. Bradshaw, F. B. Prinz and Y. Cui, *Proc. Natl. Acad. Sci. USA*, 2013, **110**, 19701-19706.
67. D. Yang, S. J. Sandoval, W. M. R. Divigalpitiya, J. C. Irwin and R. F. Frindt, *Phys. Rev. B*, 1991, **43**, 12053-12056.
68. C. G. Morales-Guio and X. Hu, *Acc. Chem. Res.*, 2014, **47**, 2671-2681.
69. D. Merki, S. Fierro, H. Vrubel and X. L. Hu, *Chem. Sci.*, 2011, **2**, 1262-1267.
70. J. D. Benck, Z. B. Chen, L. Y. Kuritzky, A. J. Forman and T. F. Jaramillo, *ACS Catal.*, 2012, **2**, 1916-1923.
71. X. Zhang, F. Meng, S. Mao, Q. Ding, M. J. Shearer, M. S. Faber, J. Chen, R. J. Hamers and S. Jin, *Energy Environ. Sci.*, 2015, **8**, 862-868.
72. M. Brorson, A. Carlsson and H. Topsoe, *Catal. Today*, 2007, **123**, 31-36.
73. J. Bonde, P. G. Moses, T. F. Jaramillo, J. K. Norskov and I. Chorkendorff, *Faraday Discuss.*, 2008, **140**, 219-231.
74. Q. Gong, L. Cheng, C. Liu, M. Zhang, Q. Feng, H. Ye, M. Zeng, L. Xie, Z. Liu and Y. Li, *ACS Catal.*, 2015, **5**, 2213-2219.
75. D. Voiry, H. Yamaguchi, J. W. Li, R. Silva, D. C. B. Alves, T. Fujita, M. W. Chen, T. Asefa, V. B. Shenoy, G. Eda and M. Chhowalla, *Nat. Mater.*, 2013, **12**, 850-855.
76. B. K. Miremadi and S. R. Morrison, *J. Appl. Phys.*, 1988, **63**, 4970-4974.
77. M. A. Lukowski, A. S. Daniel, C. R. English, F. Meng, A. Forticaux, R. J. Hamers and S. Jin, *Energ. Environ. Sci.*, 2014, **7**, 2608-2613.
78. L. Cheng, W. J. Huang, Q. F. Gong, C. H. Liu, Z. Liu, Y. G. Li and H. J. Dai, *Angew. Chem. Int. Ed.*, 2014, **53**, 7860-7863.
79. C. Tsai, K. R. Chan, F. Abild-Pedersen and J. K. Norskov, *Phys. Chem. Chem. Phys.*, 2014, **16**, 13156-13164.
80. H. T. Wang, D. S. Kong, P. Johanes, J. J. Cha, G. Y. Zheng, K. Yan, N. A. Liu and Y. Cui, *Nano Lett.*, 2013, **13**, 3426-3433.
81. M. S. Faber, M. A. Lukowski, Q. Ding, N. S. Kaiser and S. Jin, *J. Phys. Chem. C*, 2014, **118**, 21347-21356.
82. M. S. Faber, R. Dziedzic, M. A. Lukowski, N. S. Kaiser, Q. Ding and S. Jin, *J. Am. Chem. Soc.*, 2014, **136**, 10053-10061.
83. A. I. Carim, F. H. Saadi, M. P. Soriaga and N. S. Lewis, *J. Mater. Chem. A*, 2014, **2**, 13835-13839.
84. S. J. Peng, L. L. Li, X. P. Han, W. P. Sun, M. Srinivasan, S. G. Mhaisalkar, F. Y. Cheng, Q. Y. Yan, J. Chen and S. Ramakrishna, *Angew. Chem. Int. Edit.*, 2014, **53**, 12594-12599.
85. H. Zhang, B. Yang, X. Wu, Z. Li, L. Lei and X. Zhang, *ACS Appl. Mater. Interfaces*, 2015, **7**, 1772-1779.
86. W. F. Chen, J. T. Muckerman and E. Fujita, *Chem. Commun.*, 2013, **49**, 8896-8909.
87. J. R. Kitchin, J. K. Norskov, M. A. Bartaeu and J. G. Chen, *Catal. Today*, 2005, **105**, 66-73.

88. J. G. Chen, *Chem. Rev.*, 1996, **96**, 1477-1498.
89. R. B. Levy and M. Boudart, *Science*, 1973, **181**, 547-549.
90. A. L. Stottlemeyer, E. C. Weigert and J. G. Chen, *Ind. Eng. Chem. Res.*, 2011, **50**, 16-22.
91. G. Bianchi, F. Mazza and S. Trasatti, *Z. Phys. Chem.*, 1964, **226**, 40-58.
92. A. T. Garcia-Esparza, D. Cha, Y. W. Ou, J. Kubota, K. Domen and K. Takanabe, *Chemsuschem*, 2013, **6**, 168-181.
93. S. T. Hunt, T. Nimmanwudipong and Y. Roman-Leshkov, *Angew. Chem. Int. Ed.*, 2014, **53**, 5131-5136.
94. C. Wan, Y. N. Regmi and B. M. Leonard, *Angew. Chem. Int. Ed.*, 2014, **53**, 6407-6410.
95. L. Liao, S. N. Wang, J. J. Xiao, X. J. Bian, Y. H. Zhang, M. D. Scanlon, X. L. Hu, Y. Tang, B. H. Liu and H. H. Girault, *Energ. Environ. Sci.*, 2014, **7**, 387-392.
96. W. F. Chen, C. H. Wang, K. Sasaki, N. Marinkovic, W. Xu, J. T. Muckerman, Y. Zhu and R. R. Adzic, *Energ. Environ. Sci.*, 2013, **6**, 943-951.
97. L. F. Pan, Y. H. Li, S. Yang, P. F. Liu, M. Q. Yu and H. G. Yang, *Chem. Commun.*, 2014, **50**, 13135-13137.
98. D. H. Youn, S. Han, J. Y. Kim, J. Y. Kim, H. Park, S. H. Choi and J. S. Lee, *Acs Nano*, 2014, **8**, 5164-5173.
99. J. Song, G. R. Li, F. Y. Xiong and X. P. Gao, *J. Mater. Chem.*, 2012, **22**, 20580-20585.
100. W. Zheng, T. P. Cotter, P. Kaghazchi, T. Jacob, B. Frank, K. Schlichte, W. Zhang, D. S. Su, F. Schueth and R. Schloegl, *J. Am. Chem. Soc.*, 2013, **135**, 3458-3464.
101. J. Xie, S. Li, X. Zhang, J. Zhang, R. Wang, H. Zhang, B. Pan and Y. Xie, *Chem. Sci.*, 2014, **5**, 4615-4620.
102. W. F. Chen, S. Iyer, S. Iyer, K. Sasaki, C. H. Wang, Y. M. Zhu, J. T. Muckerman and E. Fujita, *Energ. Environ. Sci.*, 2013, **6**, 1818-1826.
103. W. F. Chen, K. Sasaki, C. Ma, A. I. Frenkel, N. Marinkovic, J. T. Muckerman, Y. M. Zhu and R. R. Adzic, *Angew. Chem. Int. Ed.*, 2012, **51**, 6131-6135.
104. B. F. Cao, G. M. Veith, J. C. Neufeld, R. R. Adzic and P. G. Khalifah, *J. Am. Chem. Soc.*, 2013, **135**, 19186-19192.
105. V. A. Lavrenko, L. N. Yagupol'skaya and L. I. Kuznetsova, *Elektrokhimiya*, 1974, **10**, 1078-1081.
106. P. Los and A. Lasia, *J. Electroanal. Chem.*, 1992, **333**, 115-125.
107. C. Adan, F. J. Perez-Alonso, S. Rojas, M. A. Pena and J. L. G. Fierro, *Int. J. Hydrogen Energy*, 2012, **37**, 14984-14991.
108. E. Ndzebet and O. Savadogo, *Int. J. Hydrogen Energy*, 1994, **19**, 687-691.
109. J. J. Borodzinski and A. Lasia, *J. Appl. Electrochem.*, 1994, **24**, 1267-1275.
110. H. Vrubel and X. L. Hu, *Angew. Chem. Int. Ed.*, 2012, **51**, 12703-12706.
111. S. T. Oyama, T. Gott, H. Zhao and Y.-K. Lee, *Catal. Today*, 2009, **143**, 94-107.
112. A.-M. Alexander and J. S. J. Hargreaves, *Chem. Soc. Rev.*, 2010, **39**, 4388-4401.
113. E. J. Popczun, J. R. McKone, C. G. Read, A. J. Biacchi, A. M. Wiltrot, N. S. Lewis and R. E. Schaak, *J. Am. Chem. Soc.*, 2013, **135**, 9267-9270.
114. E. J. Popczun, C. G. Read, C. W. Roske, N. S. Lewis and R. E. Schaak, *Angew. Chem. Int. Ed.*, 2014, **53**, 5427-5430.
115. J. M. McEnaney, J. C. Crompton, J. F. Callejas, E. J. Popczun, A. J. Biacchi, N. S. Lewis and R. E. Schaak, *Chem. Mater.*, 2014, **26**, 4826-4831.
116. J. M. McEnaney, J. C. Crompton, J. F. Callejas, E. J. Popczun, C. G. Read, N. S. Lewis and R. E.

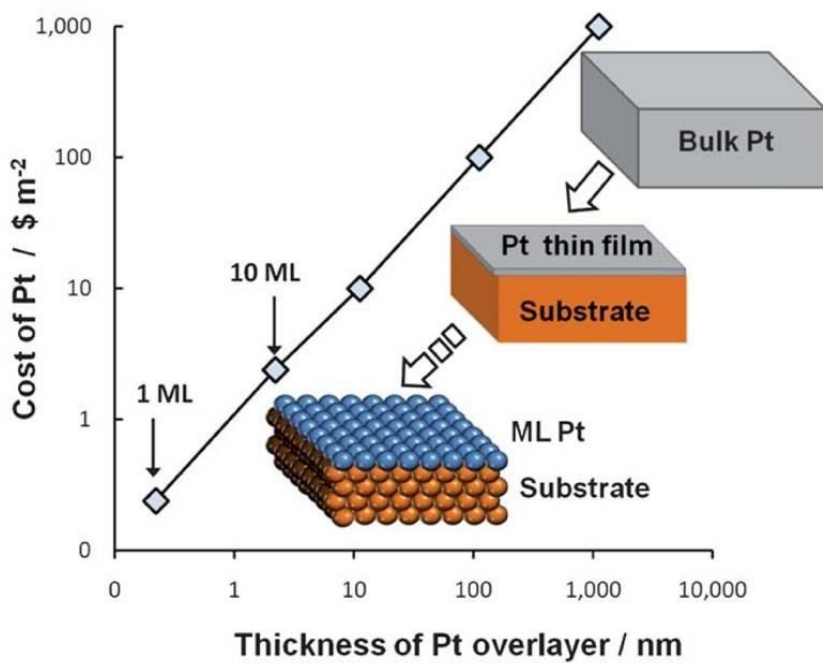
- Schaak, *Chem. Commun.*, 2014, **50**, 11026-11028.
117. L. G. Feng, H. Vrubel, M. Bensimon and X. L. Hu, *Phys. Chem. Chem. Phys.*, 2014, **16**, 5917-5921.
118. P. Jiang, Q. Liu, C. J. Ge, W. Cui, Z. H. Pu, A. M. Asiri and X. P. Sun, *J. Mater. Chem. A*, 2014, **2**, 14634-14640.
119. J. Q. Tian, Q. Liu, A. M. Asiri and X. P. Sun, *J. Am. Chem. Soc.*, 2014, **136**, 7587-7590.
120. Q. Liu, J. Q. Tian, W. Cui, P. Jiang, N. Y. Cheng, A. M. Asiri and X. P. Sun, *Angew. Chem. Int. Ed.*, 2014, **53**, 6710-6714.
121. P. Jiang, Q. Liu, Y. H. Liang, J. Q. Tian, A. M. Asiri and X. P. Sun, *Angew. Chem. Int. Ed.*, 2014, **53**, 12855-12859.
122. J. Tian, Q. Liu, N. Cheng, A. M. Asiri and X. Sun, *Angew. Chem. Int. Ed.*, 2014, **53**, 9577-9581.
123. Y. H. Liang, Q. Liu, A. M. Asiri, X. P. Sun and Y. L. Luo, *ACS Catal.*, 2014, **4**, 4065-4069.
124. P. Xiao, M. A. Sk, L. Thia, X. M. Ge, R. J. Lim, J. Y. Wang, K. H. Lim and X. Wang, *Energ. Environ. Sci.*, 2014, **7**, 2624-2629.
125. Z. C. Xing, Q. Liu, A. M. Asiri and X. P. Sun, *Adv. Mater.*, 2014, **26**, 5702-5707.
126. J. Kibsgaard and T. F. Jaramillo, *Angew. Chem. Int. Ed.*, 2014, **53**, 14433-14437.
127. Z. Pu, Q. Liu, A. M. Asiri and X. Sun, *ACS Appl. Mater. Inter.*, 2014, **6**, 21874-21879.
128. N. Daems, X. Sheng, I. F. J. Vankelecom and P. P. Pescarmona, *J. Mater. Chem. A*, 2014, **2**, 4085-4110.
129. W. Cui, Q. Liu, N. Y. Cheng, A. M. Asiri and X. P. Sun, *Chem. Commun.*, 2014, **50**, 9340-9342.
130. Y. Li, W. Zhou, H. Wang, L. Xie, Y. Liang, F. Wei, J. C. Idrobo, S. J. Pennycook and H. Dai, *Nat. Nanotechnology*, 2012, **7**, 394-400.
131. Y. Li and H. Dai, *Chem. Soc. Rev.*, 2014, **43**, 5257-5275.
132. C. E. Banks, A. Crossley, C. Salter, S. J. Wilkins and R. G. Compton, *Angew. Chem., Int. Ed.*, 2006, **45**, 2533-2537.
133. E. J. E. Stuart and M. Pumera, *J. Phys. Chem. C*, 2010, **114**, 21296-21298.
134. A. Ambrosi, S. Y. Chee, B. Khezri, R. D. Webster, Z. Sofer and M. Pumera, *Angew. Chem., Int. Ed.*, 2012, **51**, 500-503.
135. Y. Zheng, Y. Jiao, L. H. Li, T. Xing, Y. Chen, M. Jaroniec and S. Z. Qiao, *Acs Nano*, 2014, **8**, 5290-5296.
136. Y. Ito, W. Cong, T. Fujita, Z. Tang and M. Chen, *Angew. Chem. Int. Ed.*, 2014, **54**, 2131-2136.
137. M. Shalom, S. Gimenez, F. Schipper, I. Herraiz-Cardona, J. Bisquert and M. Antonietti, *Angew. Chem. Int. Ed.*, 2014, **53**, 3654-3658.
138. Y. Zheng, Y. Jiao, Y. H. Zhu, L. H. Li, Y. Han, Y. Chen, A. J. Du, M. Jaroniec and S. Z. Qiao, *Nat. Commun.*, 2014, **5**, 8.
139. Y. Zhao, F. Zhao, X. Wang, C. Xu, Z. Zhang, G. Shi and L. Qu, *Angew. Chem. Int. Ed.*, 2014, **53**, 13934-13939.
140. Y. Jiao, Y. Zheng, M. Jaroniec and S. Z. Qiao, *Chem. Soc. Rev.*, 2015, **44**, 2060-2086.
141. W. T. Hong, M. Risch, K. A. Stoerzinger, A. Grimaud, J. Suntivich and Y. Shao-Horn, *Energy Environ. Sci.*, 2015, DOI: 10.1039/C4EE03869J, Ahead of Print.
142. Q. Liu, J. Q. Tian, W. Cui, P. Jiang, N. Y. Cheng, A. M. Asiri and X. P. Sun, *Angew. Chem. Int. Edit.*, 2014, **53**, 6710-6714.
143. K. Zhang, Y. Zhao, S. Zhang, H. Yu, Y. Chen, P. Gao and C. Zhu, *J. Mater. Chem. A*, 2014, **2**, 18715-18719.
144. B. R. Sathe, X. X. Zou and T. Asefa, *Catal. Sci. Technol.*, 2014, **4**, 2023-2030.



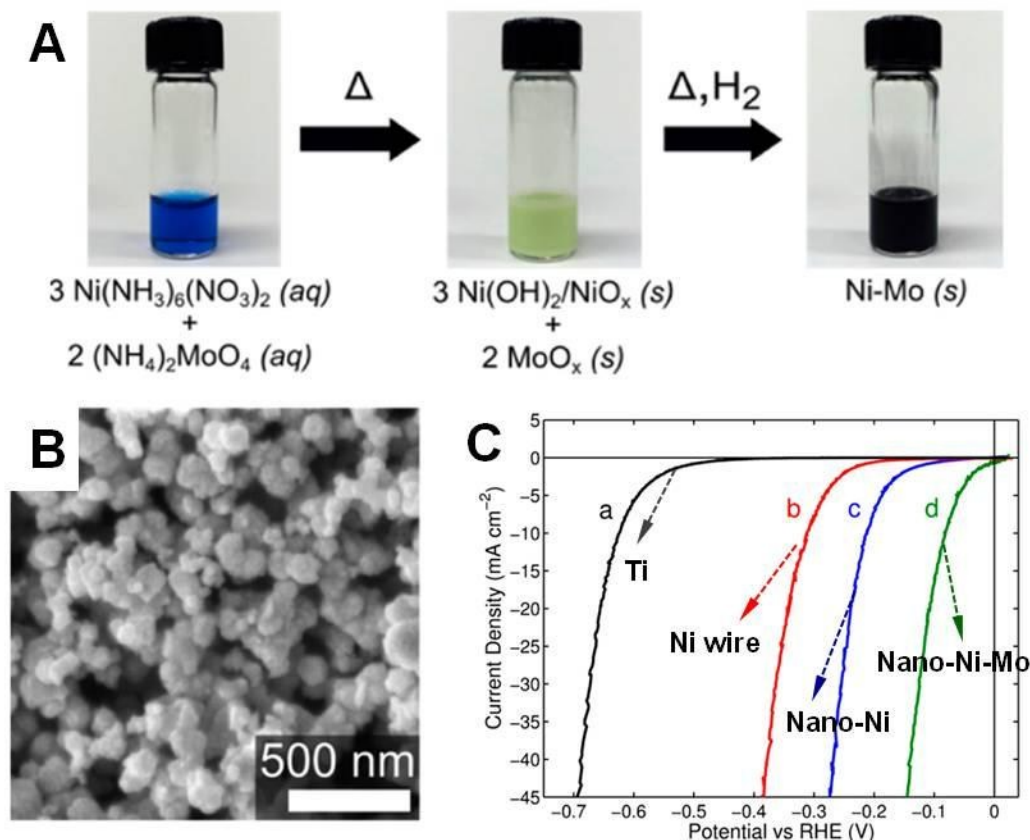
**Figure 1.** (A) Schematic illustration of the HER energetics. (B) Schematic HER polarization curves on two different electrocatalysts with their onset overpotentials indicated. (C) Schematic Tafel plots on two different electrocatalysts with their Tafel slopes and exchange current densities indicated.



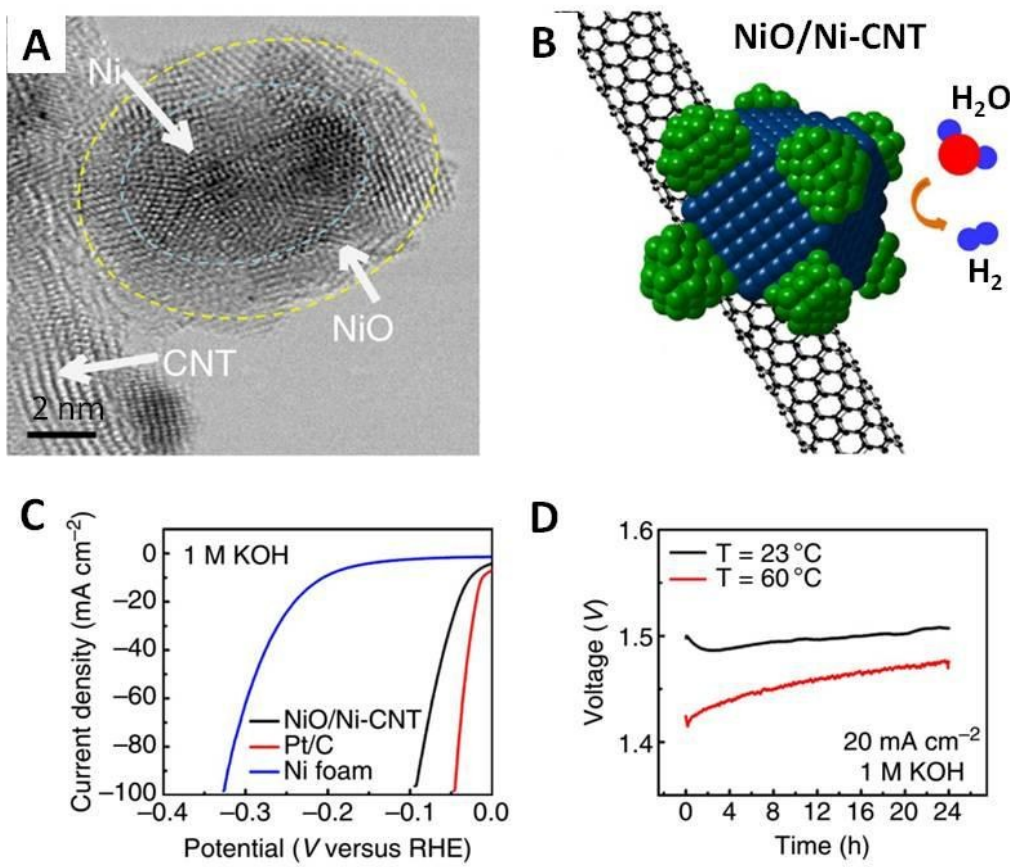
**Figure 2.** Volcano plot of exchange current density ( $j_0$ ) as a function of DFT-calculated Gibbs free energy ( $\Delta G_{H^*}$ ) of adsorbed atomic hydrogen on pure metals. Reprinted with permission from ref. 24, copyright 2005, the Electrochemical Society.



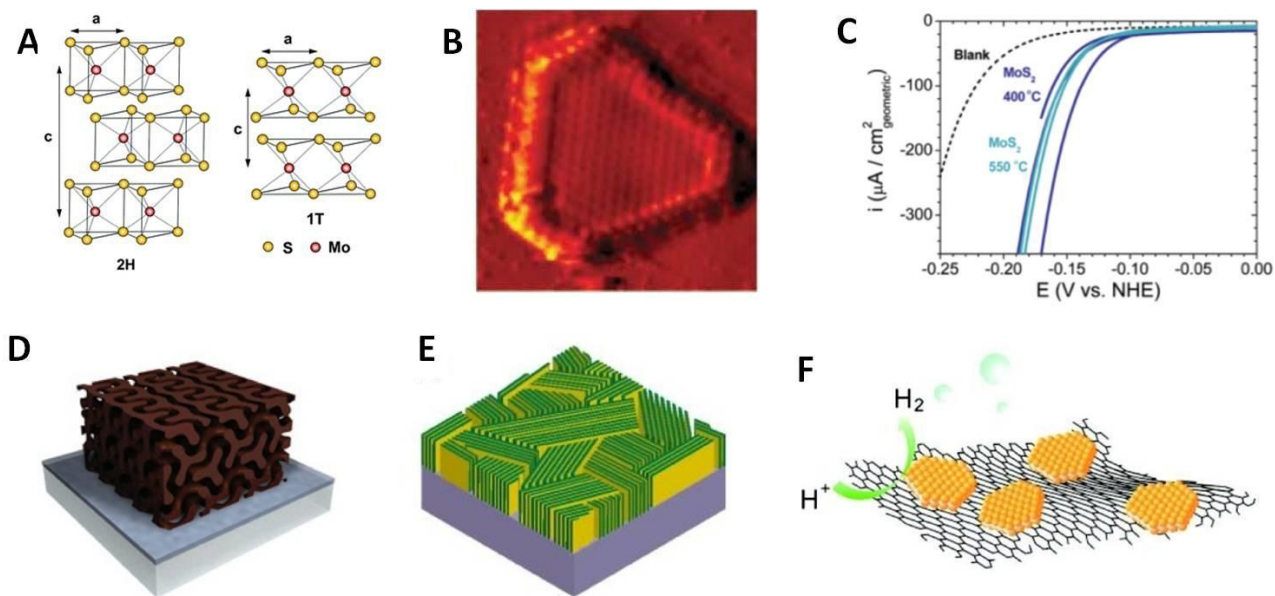
**Figure 3.** Relationship between cost of Pt and overlayer thickness for a planar catalyst configuration.  
Reprinted with permission from ref. 32, copyright 2011, Royal Society of Chemistry.



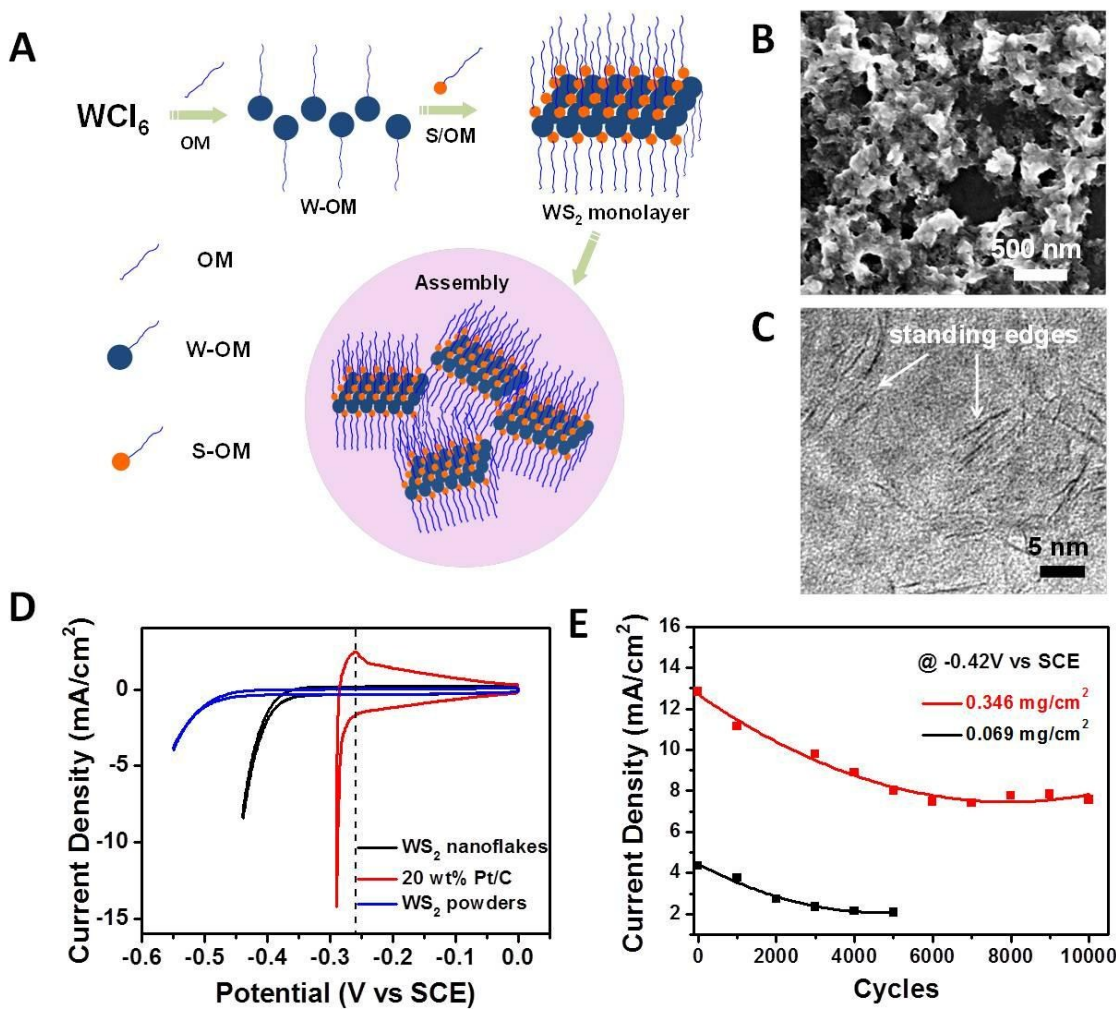
**Figure 4.** (A) Synthetic scheme for Ni–Mo nanopowders. (B) SEM image of Ni–Mo nanopowders. (C) Comparison of HER activities of four different electrodes as indicated in 1 M NaOH. Reprinted with permission from ref. 42, copyright 2013, American Chemical Society.



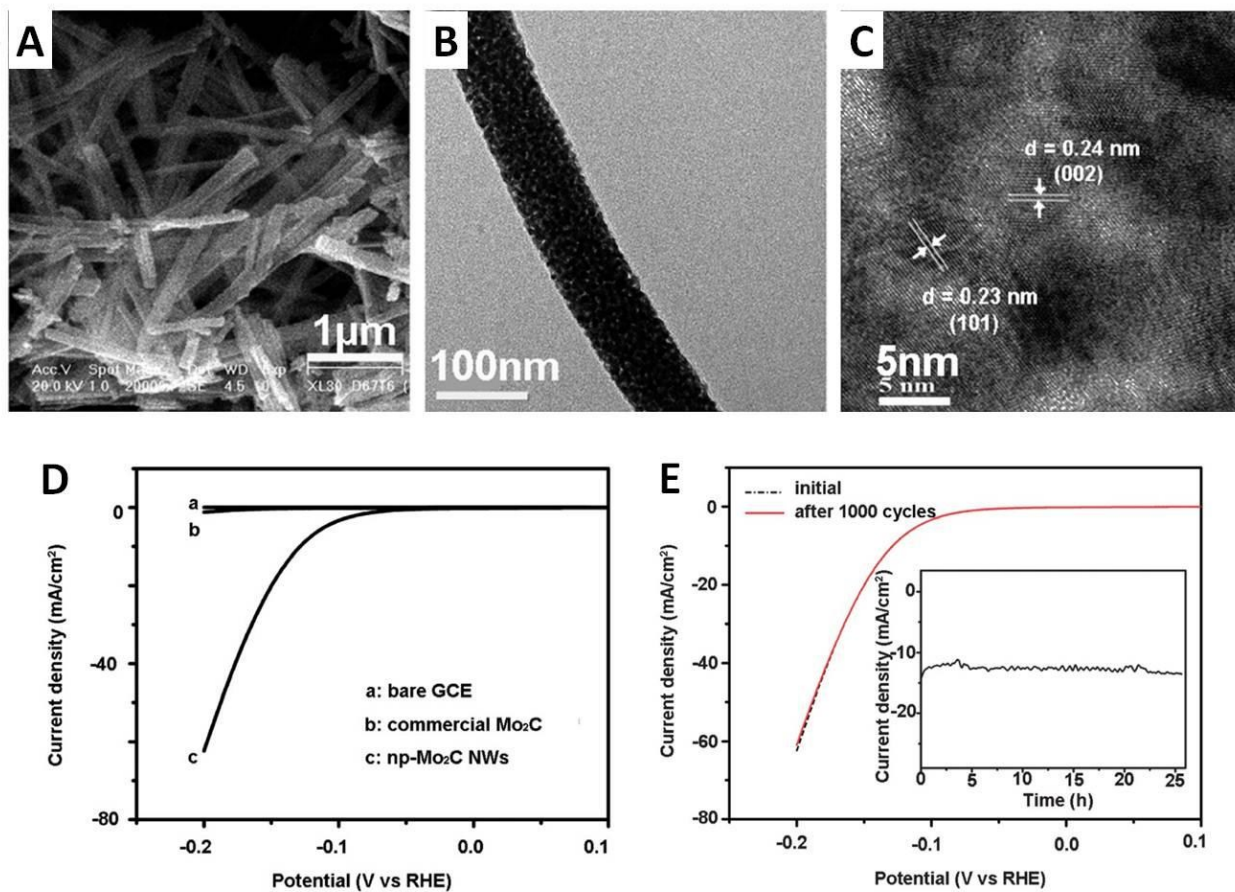
**Figure 5.** (A) Atomic resolution STEM bright-field image of the hybrid material. (B) A schematic illustration of the NiO/Ni-CNT heterostructures. (C) Linear sweep voltammetry of NiO/Ni-CNT, Pt/C deposited on Ni foam and pure Ni foam in 1 M KOH. (d) Chronopotentiometry of water electrolysis using NiO/Ni-CNT and NiFe LDH at a constant current density of 20  $\text{mA}/\text{cm}^2$  in 1 M KOH. Reprinted with permission from ref. 46, copyright 2014, Nature Publishing Group.



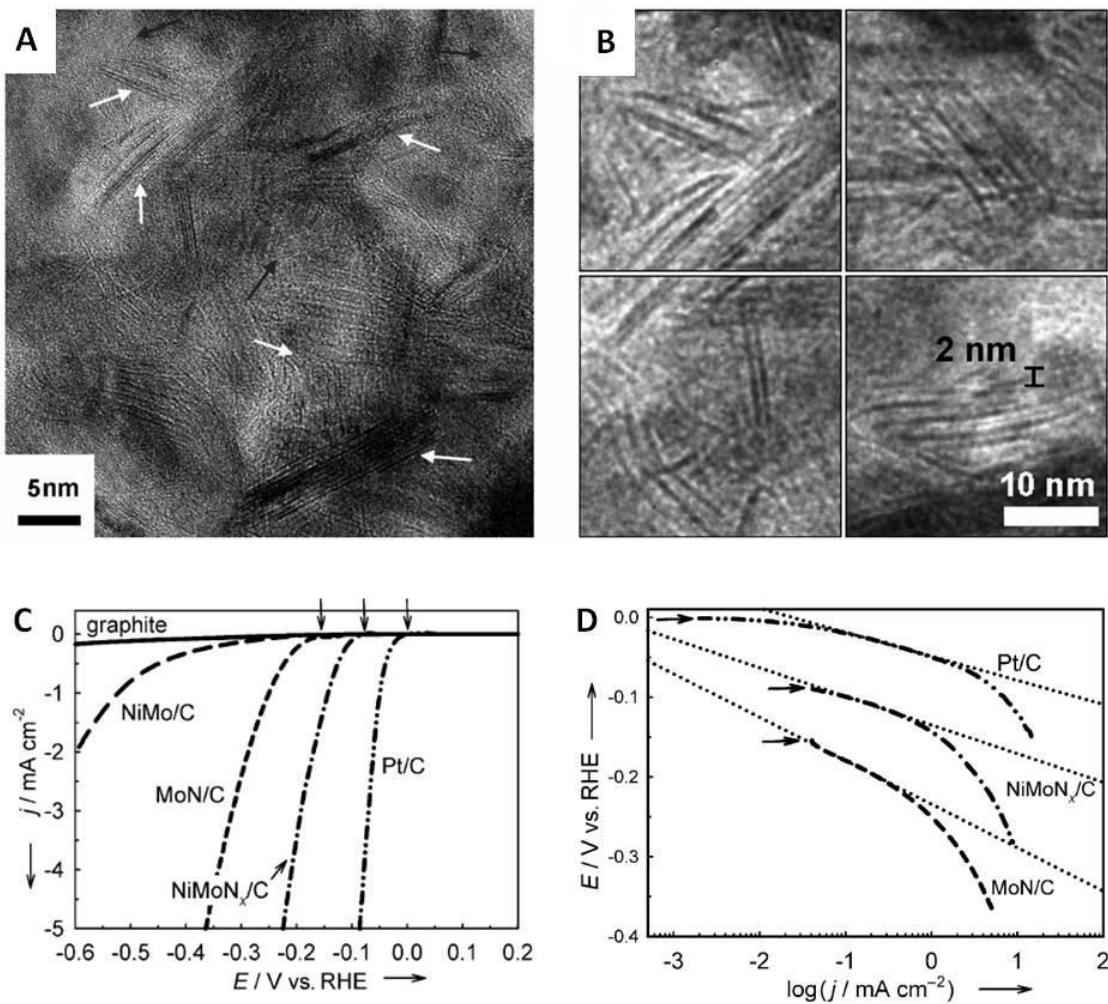
**Figure 6.** (A) Schematic crystal structure of 2H- and 1T-MoS<sub>2</sub>. Reprinted with permission from ref. 64, copyright 2012, The Royal Society of Chemistry. (B) STM image of atomically resolved MoS<sub>2</sub> nanoparticles on Au(111) and (C) their HER polarization curves. Reprinted with permission from ref. 53, copyright 2007, American Association for the Advancement of Science. (D) Schematic of double-gyroid MoS<sub>2</sub> thin film grown a substrate. Reprinted with permission from ref. 60, copyright 2012, Nature Publishing Group. (E) Schematic of edge-terminated MoS<sub>2</sub> films with the layers aligned perpendicular to the substrate. Reprinted with permission from ref. 62, copyright 2013, American Chemical Society. (F) Schematic of MoS<sub>2</sub>/graphene hybrid electrocatalyst. Reprinted with permission from ref. 63, copyright 2011, American Chemical Society.



**Figure 7.** (A) Synthetic scheme for ultrathin WS<sub>2</sub> nanoflakes. (B, C) SEM and high-resolution TEM images of WS<sub>2</sub> nanoflakes. (D) CV curve of WS<sub>2</sub> nanoflake catalyst along with those of the Pt benchmark catalyst and commercially available WS<sub>2</sub> micropowders in 0.5 M H<sub>2</sub>SO<sub>4</sub>. (E) Change in the HER cathodic current density with the number of potential cycles. Reprinted with permission from ref. 78, copyright 2014, Wiley-VCH.



**Figure 8.** (A) SEM image and (B-C) TEM images of nanoporous Mo<sub>2</sub>C nanowires (np-Mo<sub>2</sub>C NWs). (D) Polarization curve of np-Mo<sub>2</sub>C NWs compared with commercial Mo<sub>2</sub>C and bare glassy carbon electrode in 0.5 M H<sub>2</sub>SO<sub>4</sub>. (E) Polarization curve of np-Mo<sub>2</sub>C NWs before and after 1000 cycles. The inset shows its chronopotentiometric response at  $\eta = 130 \text{ mV}$ . Reprinted with permission from ref. 95, copyright 2014, Royal Society of Chemistry.



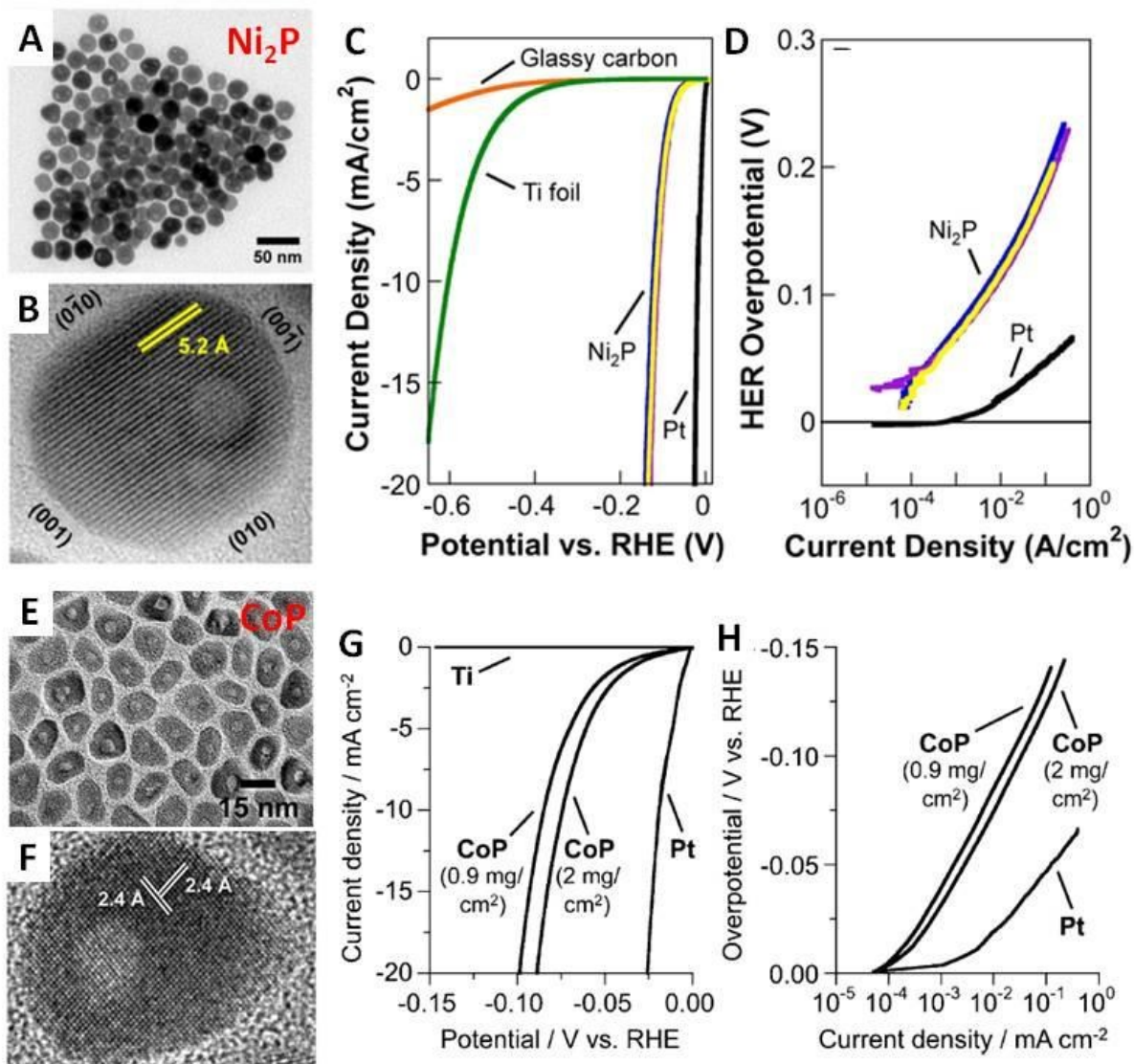


**Figure 10.** (A-B) TEM images of  $\text{Ni}_2\text{P}$  nanoparticles. (C) Polarization curves of three individual  $\text{Ni}_2\text{P}$  electrodes in  $0.5 \text{ M H}_2\text{SO}_4$ , along with glassy carbon, Ti foil, and Pt in  $0.5 \text{ M H}_2\text{SO}_4$  for comparison. (D) Corresponding Tafel plots for the  $\text{Ni}_2\text{P}$  and Pt electrodes. Above data are reprinted with permission from ref. 113, copyright 2013, American Chemical Society. (E-F) TEM images of  $\text{CoP}$  nanoparticles. (G) Polarization curves of  $\text{CoP}$  electrodes in  $0.5 \text{ M H}_2\text{SO}_4$ , along with a Ti foil and Pt for comparison. (H) Corresponding Tafel plots for the  $\text{CoP}$  and Pt electrodes. Above data are reprinted with permission from ref. 114, copyright 2014, Wiley-VCH.

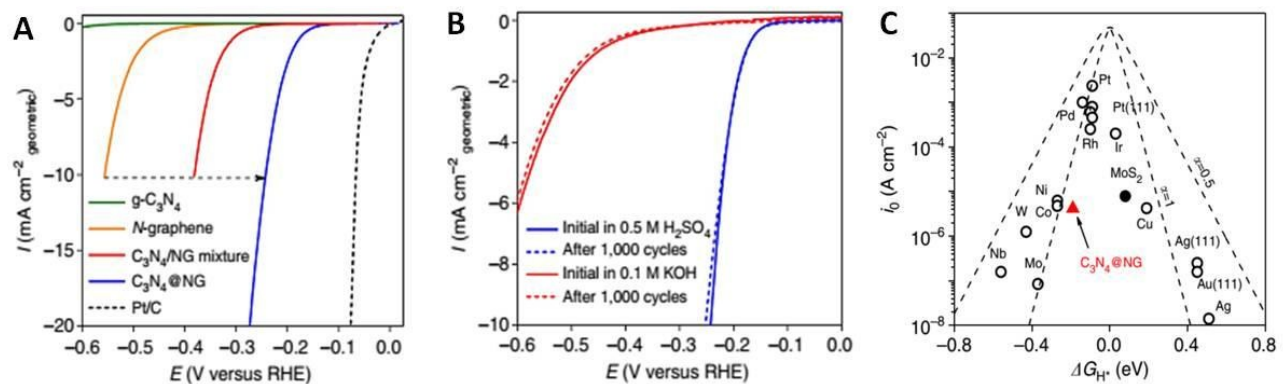


**Figure 11.** (A) HER polarization curves for four different metal-free electrocatalysts as well as Pt/C. (B) Polarization curves recorded for  $\text{C}_3\text{N}_4/\text{NG}$  hybrid before and after 1,000 potential sweeps under acidic and basic conditions. (C) Volcano plots of exchange current density as a function of calculated  $\Delta G_{\text{H}^+}$  for  $\text{C}_3\text{N}_4/\text{NG}$  (indicated by the red triangle), common metal catalysts as well as a typical MoS<sub>2</sub> catalyst. Reprinted with permission from ref. 138, copyright 2014, Nature Publishing Group.

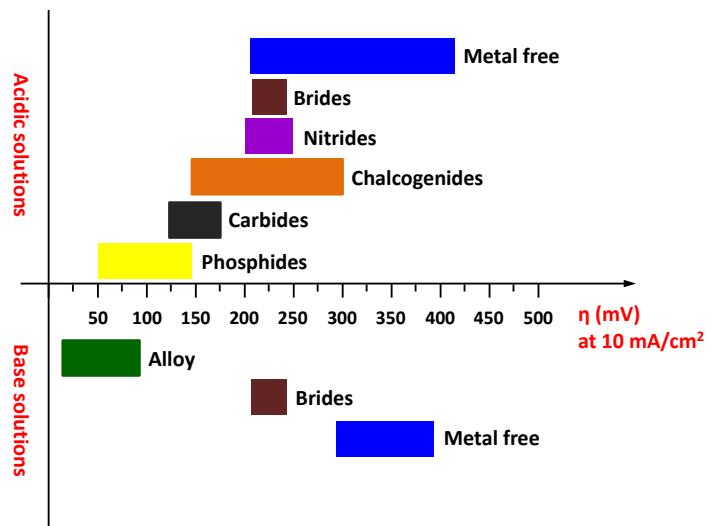


**Figure 12.** Summary and comparison of HER activities of different materials reviewed in this article.

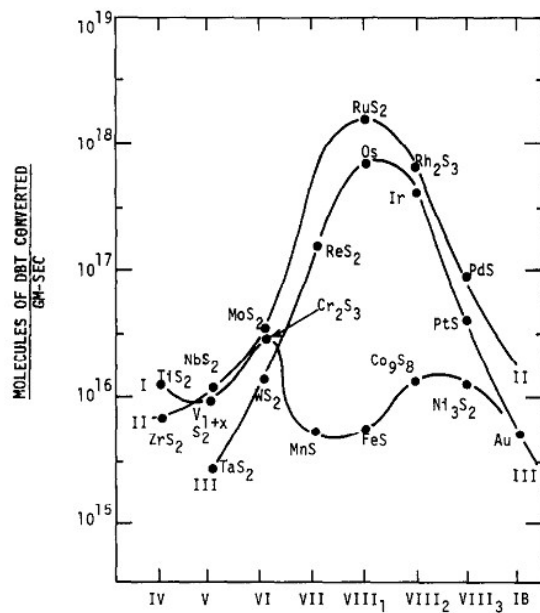
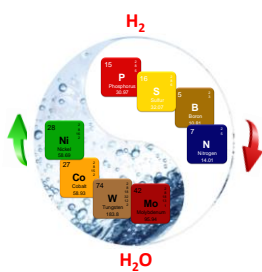


**Figure 13.** Periodic trends for HDS activities of transition metal sulfides. It can serve as a good reference in the search for new HER electrocatalysts. Reprinted with permission from ref. 51, copyright 1981, Elsevier.

TOC



In this review, the fundamental, current status and challenges of different types of HER electrocatalysts are highlighted.

**Table 1.** Summary of the performance of some HER electrocatalysts reviewed within this paper.

Materials	Electrolyte	Catalysts loading (mg/cm <sup>2</sup> )	Current density	Tafel slope (mV/decade)	Ref.
<b>Alloys</b>					
Ni-Mo electrodeposited on steel foil	6 M KOH, 80 °C	3.6	300 mA/cm <sup>2</sup> at $\eta = 185$ mV	112	13
Ni-Mo nanopowders casted on Ti foil	1 M NaOH,	1.0	10 mA/cm <sup>2</sup> at $\eta = 80$ mV	N/A	42
Ni-Mo electrodeposited on Cu foam	1 M NaOH	N/A	20 mA/cm <sup>2</sup> at $\eta = \sim 34$ mV	N/A	43
Ni/NiO-CNT hybrid on Ni foam	1 M KOH	~8	100 mA/cm <sup>2</sup> at $\eta < 100$ mV	N/A	46
CoNi/Ultrathin graphene layer	0.1 M H <sub>2</sub> SO <sub>4</sub>	1.6	10 mA/cm <sup>2</sup> at $\eta = 142$ mV	105	48
Iron nanoparticles encapsulated in single-shell carbon	0.5 M H <sub>2</sub> SO <sub>4</sub>	0.18	10 mA/cm <sup>2</sup> at $\eta = 77$ mV	40	49
<b>Chalcogenides</b>					
Double-gyroid MoS <sub>2</sub> deposited on FTO	0.5 M H <sub>2</sub> SO <sub>4</sub>	N/A	10 mV/cm <sup>2</sup> at $\eta = 260$ mV	50	60
Defect-rich ultrathin MoS <sub>2</sub> nanosheets	0.5 M H <sub>2</sub> SO <sub>4</sub>	0.285	13 mA/cm <sup>2</sup> at $\eta = 200$ mV	50	61
Vertically aligned MoS <sub>2</sub> films	0.5 M H <sub>2</sub> SO <sub>4</sub>	~0.0085	8 mA/cm <sup>2</sup> at $\eta = \sim 400$ mV	86	62
MoS <sub>2</sub> /graphene hybrid	0.5 M H <sub>2</sub> SO <sub>4</sub>	0.28	10 mA/cm <sup>2</sup> at $\eta = \sim 140$ mV	41	63
Chemically exfoliated 1T-MoS <sub>2</sub>	0.5 M H <sub>2</sub> SO <sub>4</sub>	N/A	10 mA/cm <sup>2</sup> at $\eta = \sim 187$ mV	43	65
Amorphous MoS <sub>2</sub> from electro-polymerization	1 M H <sub>2</sub> SO <sub>4</sub>	N/A	15 mA/cm <sup>2</sup> at $\eta = 200$ mV	40	69
Amorphous MoS <sub>2</sub> from a wet chemical synthesis	1 M H <sub>2</sub> SO <sub>4</sub>	N/A	10 mA/cm <sup>2</sup> at $\eta = \sim 200$ mV	60	70
Exfoliated 1T-WS <sub>2</sub> nanosheets	0.5 M H <sub>2</sub> SO <sub>4</sub>	0.0001~0.0002	10 mA/cm <sup>2</sup> at $\eta = 250$ mV	~60	75
Exfoliated 1T-WS <sub>2</sub> nanosheets	0.5 M H <sub>2</sub> SO <sub>4</sub>	~1.0	10 mA/cm <sup>2</sup> at $\eta = 142$ mV	70	77

Ultrathin WS <sub>2</sub> nanoflakes	0.5 M H <sub>2</sub> SO <sub>4</sub>	0.35	10 mA/cm <sup>2</sup> at $\eta = 160$ mV	48	78
Vertically aligned MoSe <sub>2</sub> films	0.5 M H <sub>2</sub> SO <sub>4</sub>	~0.0135	10 mA/cm <sup>2</sup> at $\eta = 250$ mV	N/A	62
Vertically aligned WSe <sub>2</sub> films on a fiber paper	0.5 M H <sub>2</sub> SO <sub>4</sub>	N/A	10 mA/cm <sup>2</sup> at $\eta = 300$ mV	77.4	80

**Carbides**

WC nanoparticles	0.5 M H <sub>2</sub> SO <sub>4</sub>	1	10 mA/cm <sup>2</sup> at $\eta = \sim 125$ mV	84	92
$\alpha$ -WC nanoparticles supported on carbon black	0.5 M H <sub>2</sub> SO <sub>4</sub>	0.724	10 mA/cm <sup>2</sup> at $\eta = \sim 160$ mV	N/A	93
Nanoporous Mo <sub>2</sub> C nanowires	0.5 M H <sub>2</sub> SO <sub>4</sub>	0.21	10 mA/cm <sup>2</sup> at $\eta = 125$ mV	53	95
$\beta$ -Mo <sub>2</sub> C nanoparticles on carbon black	0.1 M HClO <sub>4</sub>	2	10 mA/cm <sup>2</sup> at $\eta = 152$ mV	59.4	96
Mo <sub>2</sub> C/graphene hybrid	0.5 M H <sub>2</sub> SO <sub>4</sub>	0.285	10 mA/cm <sup>2</sup> at $\eta = \sim 175$ mV	54	97
Mo <sub>2</sub> C nanoparticles on carbon nanotube – graphene	0.5 M H <sub>2</sub> SO <sub>4</sub>	0.65~0.67	33.5 mA/cm <sup>2</sup> at $\eta = \sim 150$ mV	58	98

**Nitrides**

MoN nanosheets	0.5 M H <sub>2</sub> SO <sub>4</sub>	0.285	38.5 mA/cm <sup>2</sup> at $\eta = 300$ mV	90	101
Mo <sub>2</sub> N nanoparticles	0.1 M HClO <sub>4</sub>	2	10 mA/cm <sup>2</sup> at $\eta = \sim 230$ mV	N/A	102
NiMoN <sub>x</sub> /C	0.1 M HClO <sub>4</sub>	0.25	5 mA/cm <sup>2</sup> at $\eta = \sim 225$ mV	35.9	103
Nanostructured Co <sub>0.6</sub> Mo <sub>1.4</sub> N <sub>2</sub>	0.1 M HClO <sub>4</sub>	0.24	10 mA/cm <sup>2</sup> at $\eta = \sim 200$ mV	N/A	104

**Borides**

$\alpha$ -MoB microparticles	1 M H <sub>2</sub> SO <sub>4</sub> or 1 M KOH	2.3~2.5	20 mA/cm <sup>2</sup> at $\eta = 210\text{--}240$ mV	N/A	110
------------------------------	---	---------	--	-----	-----

**Phosphides**

Ni <sub>2</sub> P/Ti	0.5 M H <sub>2</sub> SO <sub>4</sub>	1	20 mA/cm <sup>2</sup> at $\eta = 130$ mV	46	113
CoP/Ti	0.5 M H <sub>2</sub> SO <sub>4</sub>	2	20 mA/cm <sup>2</sup> at $\eta = 85$ mV	50	114
WP/Ti	0.5 M H <sub>2</sub> SO <sub>4</sub>	1	20 mA/cm <sup>2</sup> at $\eta = 120$ mV	N/A	116
MoP/Ti	0.5 M H <sub>2</sub> SO <sub>4</sub>	1	10 mA/cm <sup>2</sup> at $\eta = 90$ V	45	115
Ni <sub>2</sub> P nanoparticles	1 M H <sub>2</sub> SO <sub>4</sub> 1 M KOH	0.38	20 mA/cm <sup>2</sup> at $\eta = 140$ mV 20 mA/cm <sup>2</sup> at $\eta = 250$ mV	66 102	117

CoP nanowires	0.5 M H <sub>2</sub> SO <sub>4</sub>	~0.35	10 mA/cm <sup>2</sup> at $\eta = 110$ mV	54	118
Nanoporous CoP nanowire arrays	0.5 M H <sub>2</sub> SO <sub>4</sub>	0.92	10 mA/cm <sup>2</sup> at $\eta = 67$ mV	51	119
FeP nanowire arrays	0.5 M H <sub>2</sub> SO <sub>4</sub>	3.2	10 mA/cm <sup>2</sup> at $\eta = 55$ mV	38	121
Cu <sub>3</sub> P nanowire arrays	0.5 M H <sub>2</sub> SO <sub>4</sub>	15.2	10 mA/cm <sup>2</sup> at $\eta = 143$ mV	67	122
MoP	0.5 M H <sub>2</sub> SO <sub>4</sub>	~1	30 mA/cm <sup>2</sup> at $\eta = 180$ mV	54	124
MoP nanoparticles	0.5 M H <sub>2</sub> SO <sub>4</sub>	0.36	10 mA/cm <sup>2</sup> at $\eta = 125$ mV	54	125
MoP S film	0.5 M H <sub>2</sub> SO <sub>4</sub>	3	10 mA/cm <sup>2</sup> at $\eta = 86$ mV	N/A	126

**Metal free catalysts**

Oxidized carbon nanotubes	0.5 M H <sub>2</sub> SO <sub>4</sub>	N/A	10 mA/cm <sup>2</sup> at $\eta = 220$ mV	71.3	129
N and P co-doped graphene	0.5 M H <sub>2</sub> SO <sub>4</sub>	~0.20	10 mA/cm <sup>2</sup> at $\eta = 420$ mV	91	135
N and S co-doped nanoporous graphene	0.5 M H <sub>2</sub> SO <sub>4</sub>	N/A	10 mA/cm <sup>2</sup> at $\eta = 280$ mV	80.5	136
C <sub>3</sub> N <sub>4</sub> nanorods on FTO	0.1 M KOH	N/A	0.8 mA/cm <sup>2</sup> at $\eta = 300$ mV	N/A	137
C <sub>3</sub> N <sub>4</sub> @NG	0.5 M H <sub>2</sub> SO <sub>4</sub>	~0.10	10 mA/cm <sup>2</sup> at $\eta = 240$ mV	51.5	138
C <sub>3</sub> N <sub>4</sub> nanoribbons on graphene nanosheets	0.5 M H <sub>2</sub> SO <sub>4</sub>	0.143 mg/cm <sup>-2</sup>	10 mA/cm <sup>2</sup> at $\eta = 207$ mV	54	139